

## A Panchromatic JWST Spectrum of a Giant Starspot on the Fully Convective M-dwarf TOI-3884

C. A. MURRAY <sup>1</sup>, L. GARCIA <sup>2</sup>, B. V. RACKHAM <sup>3,4</sup>, Z. BERTA-THOMPSON <sup>1</sup>, A. D. FEINSTEIN <sup>5</sup>,  
S. J. MERCIER <sup>3</sup>, B. CHARNAY <sup>6,7</sup>, L. HEBB <sup>8</sup>, J. E. LIBBY-ROBERTS <sup>9,10,11</sup>, Y. ROTMAN <sup>12</sup>, A. STEPHENS <sup>1</sup>,  
M. TIMMERMANS <sup>13,14</sup>, L. WELBANKS <sup>12</sup>, K. BARKAOU <sup>15,14,3</sup>, CALEB I. CAÑAS <sup>16,17</sup>, M. DELAMER <sup>9,10</sup>,  
E. DUCROT <sup>18,6</sup>, S. KANODIA <sup>19</sup>, S. MAHADEVAN <sup>9,10</sup>, J. P. NINAN <sup>20</sup> AND J. DE WIT <sup>3</sup>

<sup>1</sup>*Department of Astrophysical and Planetary Sciences, University of Colorado Boulder, Boulder, CO 80309, USA*

<sup>2</sup>*Center for Computational Astrophysics, Flatiron Institute, New York, NY, USA*

<sup>3</sup>*Department of Earth, Atmospheric and Planetary Sciences, Massachusetts Institute of Technology, 77 Massachusetts Avenue, Cambridge, MA 02139, USA*

<sup>4</sup>*Kavli Institute for Astrophysics and Space Research, Massachusetts Institute of Technology, Cambridge, MA 02139, USA*

<sup>5</sup>*Department of Physics and Astronomy, Michigan State University, East Lansing, MI 48824, USA*

<sup>6</sup>*LIRA, Observatoire de Paris, Université PSL, CNRS, Sorbonne Université, Université Paris Cité, 5 place Jules Janssen, Meudon, 92195, France*

<sup>7</sup>*Laboratoire d'Astrophysique de Bordeaux, Univ. Bordeaux, CNRS, B18N, allée Geoffroy Saint-Hilaire, Pessac, 33615, France*

<sup>8</sup>*Hobart and William Smith Colleges Geneva, NY 14456*

<sup>9</sup>*Department of Astronomy & Astrophysics, 525 Davey Laboratory, The Pennsylvania State University, University Park, PA 16802, USA*

<sup>10</sup>*Center for Exoplanets and Habitable Worlds, The Pennsylvania State University, University Park, PA 16802, USA*

<sup>11</sup>*Department of Physics and Astronomy, University of Tampa, Tampa, FL 34606, USA*

<sup>12</sup>*School of Earth and Space Exploration, Arizona State University, Tempe, AZ 85281, USA*

<sup>13</sup>*School of Physics & Astronomy, University of Birmingham, Edgbaston, Birmingham B15 2TT, United Kingdom*

<sup>14</sup>*Astrobiology Research Unit, Université de Liège, 19C Allée du 6 Août, 4000 Liège, Belgium*

<sup>15</sup>*Instituto de Astrofísica de Canarias (IAC), Calle Vía Láctea s/n, 38200, La Laguna, Tenerife, Spain*

<sup>16</sup>*Southeastern Universities Research Association, Washington, DC 20005, USA*

<sup>17</sup>*NASA Goddard Space Flight Center, 8800 Greenbelt Road, Greenbelt, MD 20771, USA*

<sup>18</sup>*Université Paris-Saclay, Université Paris Cité, CEA, CNRS, AIM, Gif-sur-Yvette, France*

<sup>19</sup>*Earth and Planets Laboratory, Carnegie Institution for Science, 5241 Broad Branch Road, NW, Washington, DC 20015, USA*

<sup>20</sup>*Department of Astronomy and Astrophysics, Tata Institute of Fundamental Research, Homi Bhabha Road, Colaba, Mumbai 400005, India*

### ABSTRACT

TOI-3884 b is a rare super-Neptune transiting a fully convective M dwarf that hosts a persistent giant polar spot. Because the planet occults this active region during every transit, the system offers a unique laboratory to directly probe the stellar surface and spot properties. We present seven James Webb Space Telescope (JWST) transits of TOI-3884 b observed with NIRISS and NIRSpec, spanning 0.5–5.3  $\mu\text{m}$ . While all visits show a recurring spot-crossing signature, each transit exhibits a distinct spot-crossing morphology, enabling us to infer a stellar rotation period of  $P = 11.102 \pm 0.003$  d and tightly constrain the pole-on stellar orientation ( $i_* = 40.8 \pm 0.3^\circ$ ,  $\lambda_* = 148.9 \pm 0.4^\circ$ ) and spot properties ( $R_{\text{spot}} = 0.576^{+0.006}_{-0.005} R_*$ ,  $\phi_{\text{spot}} = 84.69 \pm 0.12^\circ$ ). We leverage this orbital configuration to measure the first empirical panchromatic spectrum of an M-dwarf starspot with JWST, establishing a direct observational benchmark for stellar atmosphere models in the fully convective regime. Comparison with 1D NewEra and SPHINX atmosphere models indicates that the spot is  $185 \pm 2$  K cooler than the photosphere, consistent with previous ground-based measurements and expectations for mid-M-dwarf spot contrasts. While the models reproduce the observed contrasts at wavelengths longer than  $1 \mu\text{m}$ , they significantly underpredict the contrasts at shorter wavelengths. These results demonstrate that M-dwarf stellar atmosphere models alone may not fully capture the wavelength dependence of stellar contamination in transmission spectra and highlight the importance of empirical spot spectra for robust interpretation of planetary atmospheres, particularly in the optical.

## 1. INTRODUCTION

One of the most urgent challenges of accurately interpreting planetary transmission spectra observations around M dwarfs is dealing with stellar surface heterogeneity. Stars are speckled with cooler (spots) and hotter (faculae, plages) regions that imprint wavelength-dependent signals on transit depths, a phenomenon known as the “transit light source (TLS) effect” (B. V. Rackham et al. 2018, 2019). For low-mass stars with enhanced activity and large spot-covering fractions, the TLS effect can mask or mimic molecular features in transmission spectra (e.g., B. Rackham et al. 2017; N. Espinoza et al. 2019; O. Lim et al. 2023; E. M. May et al. 2023). Even relatively quiet M dwarfs can exhibit highly heterogeneous surfaces, as shown by photometric monitoring of slowly rotating M dwarfs (E. R. Newton et al. 2016, 2017). Furthermore, recent Hubble Space Telescope (HST) and James Webb Space Telescope (JWST; J. P. Gardner et al. 2006) studies of small exoplanets around cool stars (e.g., GJ 486 b; S. E. Moran et al. 2023, GJ 1132 b; E. M. May et al. 2023; TOI 270 d T. Mikal-Evans et al. 2023, L 98-59 c; T. Barclay et al. 2025, LHS 1140 b; C. Cadieux et al. 2024, and the TRAPPIST-1 planets; J. de Wit et al. 2016, 2018; Z. Zhang et al. 2018; O. Lim et al. 2023; N. Espinoza et al. 2025; A. Glidden et al. 2025; C. Piaulet-Ghorayeb et al. 2025; M. Radica et al. 2025; A. D. Rathcke et al. 2025; N. H. Allen et al. 2026) have struggled to definitively separate absorption from the planet’s atmosphere and from cool stellar spots.

Current mitigation strategies typically handle stellar contamination by fitting for TLS signals as a function of the temperature contrast,  $C$ , between active regions and the quiescent photosphere and the surface covering fraction of those regions,  $f$ . In practice,  $C$  is approximated using stellar atmosphere models at different temperatures to represent the photosphere and active regions. However, current 1D non-magnetic stellar models for M dwarfs (such as PHOENIX; T. O. Husser et al. 2013, SPHINX; A. R. Iyer et al. 2023, NewEra; P. H. Hauschildt et al. 2025) exhibit discrepancies (A. R. Iyer & M. R. Line 2020; B. V. Rackham & J. De Wit 2024) that can lead to inconsistent atmospheric inferences (O. Lim et al. 2023) and often are poor match to empirical spectra (H. R. Wakeford et al. 2019; L. J. Garcia et al. 2022; F. Davoudi et al. 2024). Recent 3D magnetohydrodynamic (MHD) simulations of M dwarfs offer

some hope of reconciling some of these disparities (H. N. Smitha et al. 2025), but these predictions remain largely untested against empirical panchromatic measurements. The absence of direct starspot spectra for M dwarfs is therefore a critical gap in interpreting transmission spectra in the JWST era.

Spot-crossing events provide a direct observational pathway to address this problem (B. V. Rackham et al. 2023). When a planet transits over an active feature, the resulting light curve signature can constrain the spot’s size, location, and spectral contrast (e.g., K. F. Huber et al. 2010; D. K. Sing et al. 2011; F. Pont et al. 2013; L. Mancini et al. 2017; B. M. Morris et al. 2017; N. Espinoza et al. 2019). If the spots share a common temperature, these events in turn reveal information about the unocculted stellar surface, enabling an empirical estimate of TLS signals as a necessary benchmark for theoretical models and as a physically grounded foundation for TLS corrections.

TOI-3884 b offers a uniquely powerful laboratory for probing M-dwarf spot spectra. The planet is a short-period ( $P=4.54$  d) super-Neptune ( $6.4 \pm 0.2 R_{\oplus}$ ,  $32.6 \pm 7.3 M_{\oplus}$ ) transiting a nearby ( $d=43$  pc) fully convective M dwarf ( $M=0.30 M_{\odot}$ ,  $T_{\text{eff}}=3180 \pm 88$  K; G. Chabrier & I. Baraffe 1997; J. E. Libby-Roberts et al. 2023). All observed transits exhibit a large, repeatable spot-crossing anomaly (J. M. Almenara et al. 2022; J. E. Libby-Roberts et al. 2023), while long-term photometry shows minimal, though detectable, rotational modulation (P. Tamburo et al. 2025; M. Mori et al. 2025). Together, these observations indicate a nearly pole-on stellar inclination and a long-lived, near-polar active region that is occulted during every transit (J. E. Libby-Roberts et al. 2023; M. Mori et al. 2025; P. Tamburo et al. 2025; H. Chakraborty et al. 2025; S. Sagynbayeva et al. 2025). Though spots are common on fully convective M dwarfs (E. R. Newton et al. 2016, 2017), such a polar geometry is exceptionally rare for transiting exoplanets: it virtually guarantees spot occultations and allows the planet to repeatedly probe the same active region. The result is a natural laboratory for empirically measuring the spectral properties of a starspot on a fully convective M dwarf.

Giant planets are intrinsically rare around low-mass M-dwarf stars (G. Laughlin et al. 2004; S. Ida & D. N. C. Lin 2005; J. C. Morales et al. 2019; R. Burn et al. 2021) — TOI-3884 b is the only known super-Neptune planet to orbit a fully convective M dwarf (cooler than 3300 K or smaller than  $0.35 M_{\odot}$ ; G. Chabrier & I. Baraffe 1997). Their deep transits and strong atmospheric features make these planets sensitive probes of ongoing atmospheric processes (e.g. aerosol formation, disequilibrium

Visit	Date	Time [d]	Instrument	$N^*$
1	16 Dec 2024	60660.2	NIRISS/SOSS	1
2	20 Dec 2024	60664.7	NIRSpec/G395M	2
3	25 Dec 2024	60669.3	NIRISS/SOSS	3
4	29 Dec 2024	60673.9	NIRSpec/G395M	4
5	24 May 2025	60819.3	NIRSpec/G395H	36
6	02 June 2025	60828.3	NIRISS/SOSS	38
7	15 June 2025	60842.0	NIRISS/SOSS	41

\* Transit number  $N$  from the first JWST observation.

**Table 1.** Dates and instrument modes for the seven JWST visits from the GO-5863 and GO-5799 programs. Throughout this work times are defined in BJD TDB - 2400000.5 d.

chemistry, or atmospheric escape) and characterizing their atmospheres accurately can help us understand an extreme limit of gas giant formation and evolution.

In this Letter, we present seven JWST transit observations of TOI-3884 b spanning 0.5–5.3  $\mu\text{m}$  and use the recurrent spot-crossing anomalies to derive the first empirical panchromatic spectrum of a starspot on a fully convective M dwarf. Section 2 describes the observations and data reductions. In Section 3, we derive wavelength-independent stellar and orbital parameters from the NIRSpec data, followed by a self-consistent joint model of the six visits least impacted by flares in Section 4 to constrain the stellar orientation and rotation and spot geometry. We cross-check our results by performing individual visit fits in Section 5. We present the resulting spot contrast spectrum and compare it to stellar models in Section 6, place our results in broader context in Section 7, and summarize our conclusions in Section 8.

## 2. OBSERVATIONS AND DATA REDUCTION

### 2.1. James Webb Space Telescope Observations

We combine seven transit observations of TOI-3884 b from JWST Cycle 3 programs GO-5863 (PI: Murray) and GO-5799 (PI: Garcia, co-PIs: Rackham, Timmermans, Charnay)<sup>21</sup>, summarized in Table 1. Due to the similarity in science goals and observing strategy between the programs, we opted to combine teams and observations to produce a more powerful dataset.

#### 2.1.1. GO-5863

In the GO-5863 program, we observed four consecutive transits of TOI-3884 b, alternating between the Near-Infrared Imager and Slitless Spectrograph

(NIRISS; R. Doyon et al. 2023) in Single Object Slitless Spectroscopy (SOSS) mode (Visit 1: 16 Dec 2024, Visit 3: 25 Dec 2024) and the Near-Infrared Spectrograph (NIRSpec; P. Jakobsen et al. 2022) in Bright Object Time (BOTS) mode with the G395M grating (Visit 2: 20 Dec 2024, Visit 4: 29 Dec 2024).

For NIRISS/SOSS, we utilized the GR700XD disperser with the SUB256 subarray and NISRAPID readout pattern. We used 10 groups/integration (60.4 s/integration, 96 integrations in-transit) to remain below  $\sim 80\%$  of saturation while maintaining a cadence sufficient to resolve short-timescale stellar variability. Each visit consisted of 251 science integrations over  $\sim 4.2$  hour, corresponding to the transit duration (1.60 hour) with an equal amount of out-of-transit baseline plus an additional 1 hour buffer for scheduling flexibility and instrument settling. Target acquisition was performed with SOSSFAINT and 19 groups.

For NIRSpec, we used BOTS mode with the G395M grating, F290LP filter, S1600A1 slit ( $1.6'' \times 1.6''$ ), SUB2048 subarray, and NRSRAPID readout pattern. We observed 23 groups/integration, giving 21.6 s/integration and 267 integrations in-transit. For target acquisition we relied on JWST’s natural pointing ( $\sim 0.1$  arcsec radial, well within the aperture of the  $1.6'' \times 1.6''$  S1600A1 slit) due to the lack of suitable unsaturated reference sources within the visit splitting distance.

#### 2.1.2. GO-5799

In the GO-5799 program, we observed three transits of TOI-3884 b: one with NIRSpec-G395H (Visit 5: 24 May 2025), followed by two with NIRISS-SOSS (Visit 6: 02 June 2025, Visit 7: 15 June 2025).

The NIRISS/SOSS observations used the same setup as in GO-5863, with 10 groups/integration. Each visit consisted of 321 integrations, yielding a total exposure time of 5.4 hr per visit. Target acquisition was performed on TOI-3884 using the SOSSFAINT mode with the F480M filter, NISRAPID readout pattern, and 3 groups.

The NIRSpec observation followed the same BOTS mode setup at GO-5863 but with the G395H grating. To remain below  $\sim 80\%$  of saturation, we used 70 groups per integration, resulting in 303 integrations and a total exposure time of 5.4 hr. Target acquisition was performed using the Wide Aperture Target Acquisition (WATA) mode.

<sup>21</sup> All the JWST data used in this paper can be found in MAST: <https://doi.org/10.17909/bn1d-sz91>.

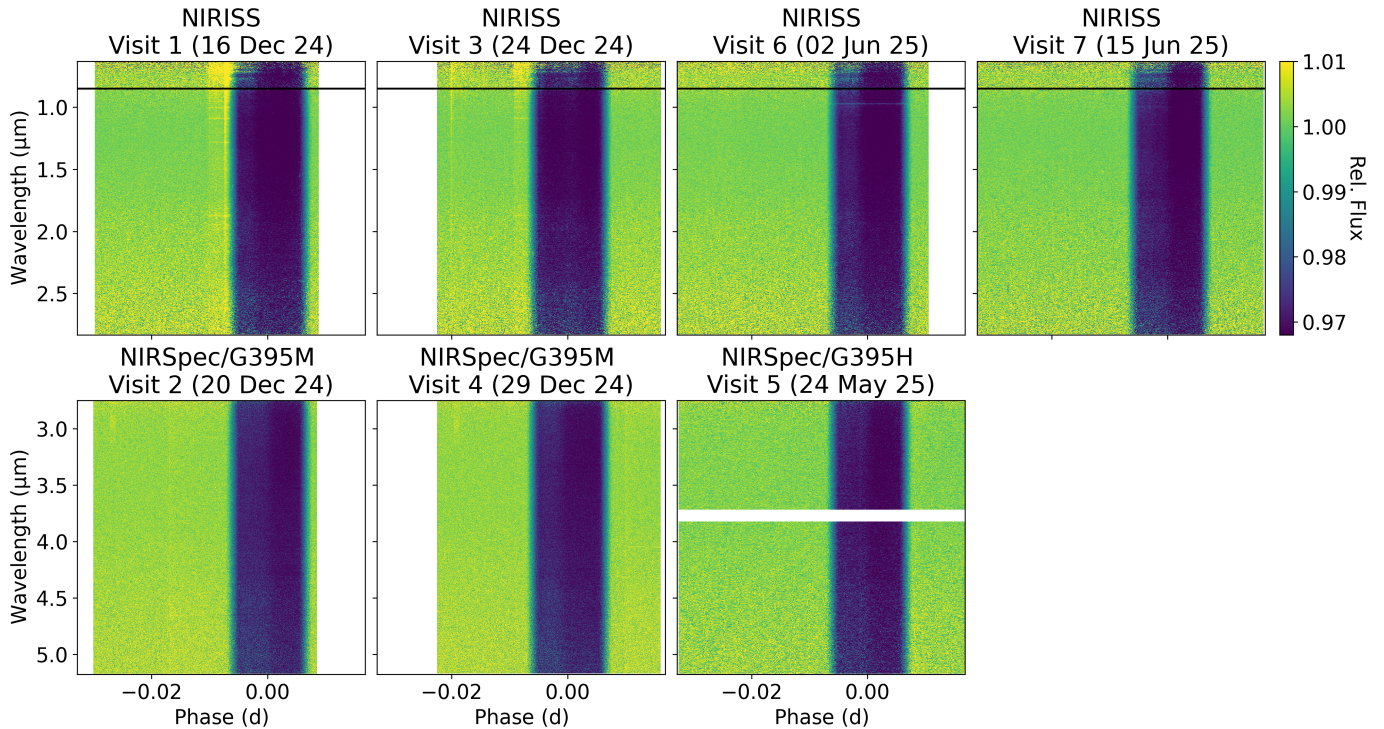


**Figure 1.** Spectroscopic time-series of the transit light curves of TOI-3884 b for all seven JWST visits, reduced with ExoTDRF (Section 2.2). NIRISS/SOSS observations are presented in the top row, and NIRSpec/BOTS in the bottom. Each panel shows normalized flux as a function of orbital phase and wavelength, and the color scale is shared across all panels. In all visits, the planetary transit appears as a broad vertical band centered at phase zero, and the spot-crossing event is apparent in the first half of the transit. Several visits also exhibit continuum and line emission attributable to stellar flares. The horizontal black lines ( $0.85\ \mu\text{m}$ ) on the top panels indicate approximately where NIRISS orders 1 and 2 overlap ( $0.85\text{--}1.10\ \mu\text{m}$ ). The white horizontal bar in Visit 5 indicates the gap between the NRS1 and NRS2 detectors for the G395H mode ( $3.72\text{--}3.82\ \mu\text{m}$ ); in G395M mode only NRS1 is illuminated.

## 2.2. Data Reduction

All visits were reduced independently using two pipelines: Eureka! (v1.2, T. J. Bell et al. 2022)<sup>22</sup> and ExoTDRF (formerly supreme-SPOON, A. D. Feinstein et al. 2023; M. Radica et al. 2023; M. Radica 2024)<sup>23</sup>. The two reductions yielded consistent spectroscopic light curves within uncertainties; unless otherwise noted, we adopt the ExoTDRF reductions for subsequent analysis. We briefly summarize these reductions here and provide full reduction details in Appendix A.

Eureka! performs detector-level corrections using the JWST calibration pipeline followed by time-series-optimized extraction. We applied standard Stage 1 and 2 calibrations, including ramp fitting, dark subtraction, flat-fielding, and wavelength calibration, with adjustments appropriate for time-series data (e.g., group-level background correction and tuned jump rejection thresholds). Spectra were extracted using optimal extraction

after trace identification and background subtraction. NIRSpec/G395H NRS1 and NRS2 data were reduced separately.

ExoTDRF provides an independent end-to-end reduction framework for JWST exoplanet time series. We performed standard detector calibrations using the JWST pipeline, including superbias subtraction, dark correction, flat-fielding, and wavelength calibration. For NIRISS/SOSS, we scaled and subtracted the STScI background model and applied a group-level  $1/f$  noise correction. For NIRSpec, additional integration-level  $1/f$  correction and wavelength adjustments were applied as needed. Spectra were extracted using box apertures optimized for each instrument mode.

## 2.3. Qualitative Behavior of the Reduced Light Curves

Figures 1 and 2 present the reduced JWST transit light curves of TOI-3884 b, shown respectively as spectroscopic and white-light time series for all seven visits. In all visits, a prominent spot-crossing event is apparent during the first half of the transit, suggesting the polar spot persists over the full observational baseline. The timing, width, and detailed morphology of the feature

<sup>22</sup> <https://eureka.readthedocs.io/en/latest/>

<sup>23</sup> <https://exotdrf.readthedocs.io/en/latest/>

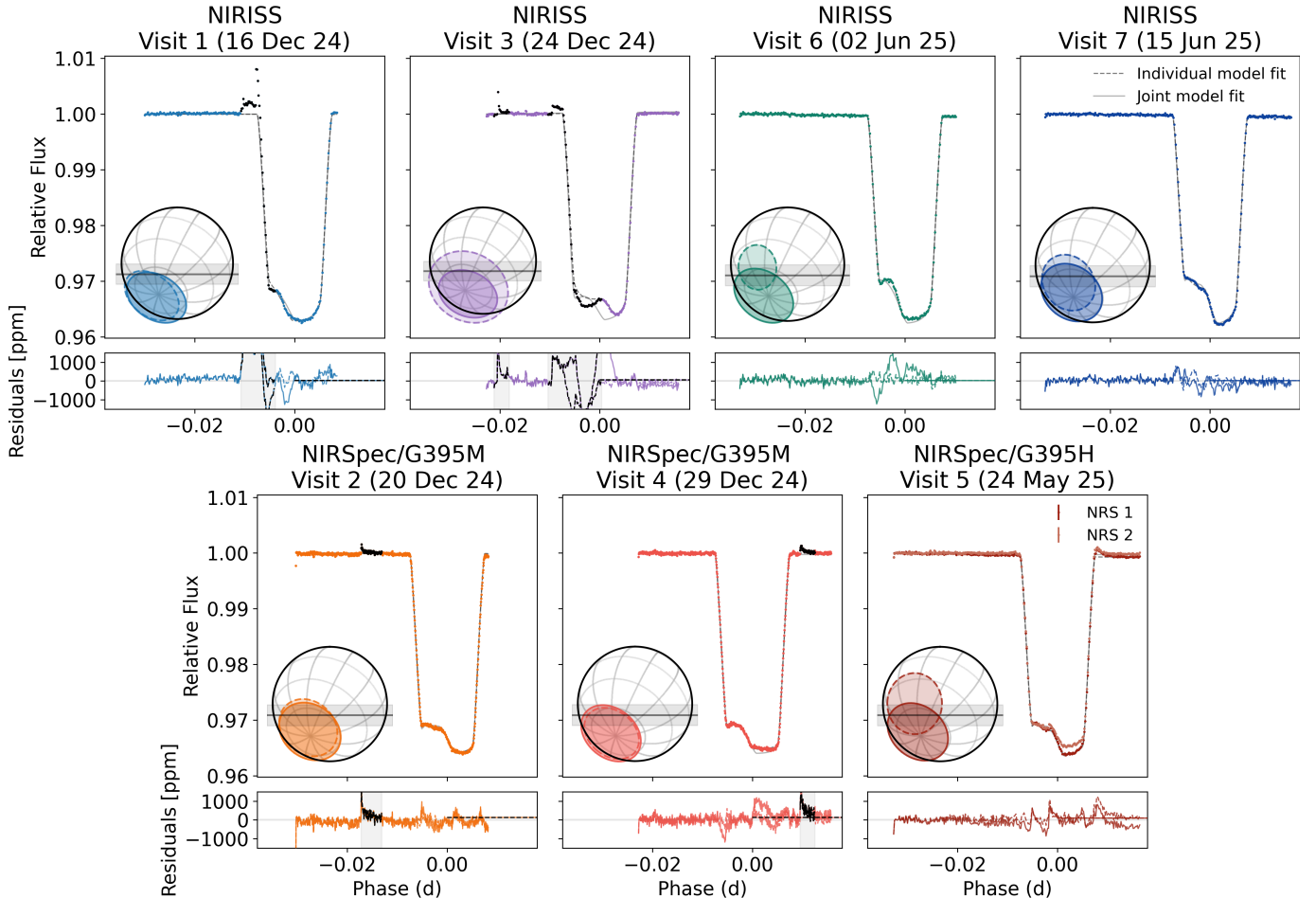


**Figure 2.** White-light transit light curves of TOI-3884 b for all seven JWST visits using the ExoTDRF reduction described in Section 2.2. NIRISS/SOSS observations are presented in the top row, and NIRSpec/BOTS in the bottom. For each visit, the upper panel shows the normalized flux as a function of transit phase as well as the best-fitting white-light models for each visit independently (Section 5, dashed lines), and for the six fits jointly (Section 4, solid lines). We plot how the respective individual and joint spot fits for each visit would look on TOI-3884 in each panel. The lower plots show the corresponding flux residuals for both models. All visits exhibit a pronounced spot-crossing feature during the first half of the transit, though its shape clearly varies between visits. Stellar flares are evident in most light curves to some degree. Visits 1 and 3, in particular, show strong stellar flares that overlap the transit window. The NIRSpec observations, which probe longer wavelengths, show comparatively quiescent behavior, though flares are still present in all NIRSpec datasets. All flares that are masked during light curve fitting are highlighted in black (with corresponding gray shaded regions shown in the residuals).

vary between visits, suggesting changes in the projected location of the occulted region due to stellar rotation and possible substructure or intrinsic evolution within the active region.

Several visits also show clear signatures of stellar flaring. Visits 1–5 exhibit flares before, during, or after transit (Figure 2), with the first two NIRISS observations (Visits 1 and 3) particularly affected by strong pre-ingress outbursts of multiple flares that extend into transit. Visit 3 has an unusual flare shape, characterized by a sharp rise followed by an approximately linear decline rather than the usual exponential decay. This may reflect overlapping flare events, including one that occurs during ingress (around  $t=60669.42$  d in Figure

6). The NIRISS bandpass covers a number of chromospheric activity indicators—such as  $H\alpha$  ( $0.656 \mu\text{m}$ ), several Paschen (H8-3,  $0.9546 \mu\text{m}$ , H7-3,  $1.005 \mu\text{m}$ , H6-3,  $1.094 \mu\text{m}$ , H5-3,  $1.282 \mu\text{m}$ , H4-3,  $1.875 \mu\text{m}$ ) and Brackett (H8-4,  $1.944 \mu\text{m}$ ) lines, and the He I and Ca II infrared triplets ( $1.0833 \mu\text{m}$  and  $0.85\text{--}0.87 \mu\text{m}$  respectively)—which show enhanced emission during flares, confirming their stellar nature. The  $H\alpha$  light curves for Visits 1 and 3 are shown in Figure 6.

Visit 6 (02 June 2025) has a zeroth-order contaminant overlapping Order 1 at  $\lambda \approx 0.96\text{--}0.985 \mu\text{m}$  in the raw images. This contamination sharply reduces the transit depth at these wavelengths (Figure 1). We mask this region in our spectroscopic light curves.

Aside from a lower first integration in several visits, the white light curves show no significant ramps or long-term slopes (Figure 2). We therefore do not include any polynomial systematics models in our transit fits.

### 3. EXTRACTING ORBITAL PARAMETERS

To determine wavelength-independent stellar and orbital parameters, we fit only the three JWST/NIRSpec visits (2, 4, and 5). The effect of limb-darkening and the contrasts between flares, spots and the stellar photosphere all decrease towards redder wavelengths, meaning that NIRSpec observations ( $\lambda=3.0\text{--}5.3\ \mu\text{m}$ ) are significantly less impacted by the star than for NIRISS, yielding more accurate orbital parameters.

#### 3.1. Combining the NIRSpec Visits

Visits 2 and 4 used the medium-resolution G395M grating, while Visit 5 was observed with the higher-resolution G395H grating. To combine all NIRSpec visits consistently, we extracted only the G395H NRS1 wavelength range ( $2.75\text{--}3.72\ \mu\text{m}$ ) for our first two visits, essentially creating mock NRS1 light curves. We then binned, normalized, and combined all three visits into a single white light curve for joint modeling.

#### 3.2. Treatment of NIRSpec Flares

All three NIRSpec observations exhibit minor flare events. Visit 2 shows one pre-transit flare, Visit 4 one post-transit, and Visit 5 two small flares: one during the spot-crossing and one post-egress. The flares in Visit 5 are independently confirmed in simultaneous Gemini/GMOS observations (Program GN-2025A-DD-108, PI Murray; Stephens et al. in prep).

We masked the out-of-transit flares in Visits 2 and 4 to reduce the number of fitted parameters. For Visit 5, we modeled both small, in-transit flares to save precious in-transit data. We use the G. T. Mendoza et al. (2022) template to model flares as a convolution of a Gaussian with a double exponential. We fit both flares for their epochs  $t_{\text{flare}}$ , amplitudes  $A_{\text{flare}}$ , and full-width half-maximums (FWHMs)  $\Delta t_{\text{flare}}$ , simultaneously with the transit and spot parameters described in the following sections (Table 2).

#### 3.3. Fitting Spot Crossings

We modeled all spot-crossing events using the Python tool `fleck` (B. Morris 2020), similarly to M. Mori et al. (2025). `fleck` simulates starspots as circular dark regions on the surfaces of rotating stars, accounting for limb darkening, limb foreshortening, and rotational modulation. `fleck` is usually recommended for smaller

spots due to known edge effects near the stellar limb<sup>24</sup>, and we discuss the impact of this limitation in Section 7.3. `fleck`, like most spot-fitting models, also neglects the impact of differential limb-darkening across spots.

#### 3.4. Parallel-Tempered Sampling

Spot properties are inherently degenerate. Geometric symmetries above and below the transit chord and different spot configurations can produce nearly identical light curve signatures, resulting in a highly multi-modal posterior. Standard MCMC methods can get stuck in local maxima in such cases (D. Foreman-Mackey et al. 2013; D. W. Hogg & D. Foreman-Mackey 2018; Section 6.3 of J. Dunkley et al. 2005).

To mitigate this, we utilized parallel-tempering MCMC, which runs ensembles of Markov chains at different “temperatures,” effectively flattening the likelihood at higher temperatures to enable efficient exploration of parameter space (R. H. Swendsen & J.-S. Wang 1986; C. J. Geyer 1991; D. J. Earl & M. W. Deem 2005; W. D. Vousden et al. 2016). Periodic swaps between chains further improve mixing across modes. Following S. Sagynbayeva et al. (2025), we implemented this approach using `ptemcee`, an adaptation of `emcee` (D. Foreman-Mackey et al. 2013) that incorporates dynamic temperature selection following W. D. Vousden et al. (2016).

#### 3.5. Best-Fit Wavelength-Independent Parameters

We modeled the combined NIRSpec white light curve using `batman` (L. Kreidberg 2015) for the planetary transit and `fleck` for the stellar surface. As the spot-crossing structure evolves between visits we included spot rotation in this fit. To reduce dimensionality, we fixed the stellar rotation period to  $P_{\text{rot}}=11.020\ \text{d}$ , from P. Tamburo et al. (2025), while using `ptemcee` to simultaneously fit for the stellar (inclination  $i_*$  and sky-projected obliquity  $\lambda_*$ ), orbital (planet-to-star radius ratio  $R_p/R_*$ , period  $P_{\text{orb}}$ , semi-major axis  $a/R_*$ , epoch  $t_0$ , and inclination  $i$ ), spot (radius  $R_{\text{spot}}$ , latitude  $\phi_{\text{spot}}$ , longitude  $\lambda_{\text{spot}}$ , and contrast  $C$ ), and flare parameters. Priors and posterior values are summarized in Table 2.

As we normalized each visit before combining, we included a separate flux scaling parameter for each visit ( $p_{2,0}$ ,  $p_{4,0}$ ,  $p_{5,0}$ ) to absorb offsets due to stellar rotation not captured by the normalization. Similarly to P. Tamburo et al. (2025), we restricted the stellar inclination to a uniform prior between  $0\text{--}90^\circ$ , while we allowed the sky-projected obliquity to vary  $0\text{--}360^\circ$ , permitting the stellar pole to be anywhere on the visible hemisphere.

<sup>24</sup> <https://fleck.readthedocs.io/en/stable/fleck/details.html>

We also included an uncertainty inflation parameter,  $\sigma_{\text{infl}}$ , added in quadrature to the reported uncertainties to account for residual systematics and model incompleteness.

We tuned the adaptation time and lag in `pemcee` to 10 and 100 respectively. Sampling was performed with 25 temperatures and 50 walkers. After a burn-in of 80000 steps, chains were run for an additional 5000 steps. All chains exceeded 50 times the integrated autocorrelation time, indicating convergence<sup>25</sup>.

#### 4. JOINT LIGHT CURVE ANALYSIS

To construct a global spot model for TOI-3884, we performed a joint analysis of multiple JWST visits, allowing us to constrain the stellar inclination, sky-projected obliquity, rotation period, and spot parameters within a self-consistent rotating framework. We used `fleck`, which explicitly models spots on a rotating stellar surface.

##### 4.1. Masking NIRISS Flares

In addition to the three NIRSpec flares described in Section 3.2, the first two NIRISS visits exhibit large flare outburst events pre-ingress (see Figure 2). These events display complex, unusual morphologies (Figure 6), making it difficult to identify individual flares or determine how many flare components to model. Additionally the flare tails overlap with the transit and spot-crossing signal, further complicating joint modeling. Therefore, we excluded Visit 3 from the joint fit as the large flare outburst spans most of transit (Figure 1), as indicated in the activity tracer H $\alpha$  (Figure 6), preventing reliable separation of flare and spot signals. Visit 1 also shows flare activity; however, the H $\alpha$  emission dissipates throughout the spot-crossing. Therefore, we included Visit 1 but masked the flaring event.

##### 4.2. White-Light Fit

To model the joint white light curves we fixed the wavelength-independent stellar and planetary parameters to the results from the NIRSpec joint fit (Table 2), while simultaneously fitting for the spot parameters ( $R_{\text{spot}}$ ,  $\phi_{\text{spot}}$  and  $\lambda_{\text{spot}}$ ), stellar rotation and geometry ( $P_{\text{rot}}$ ,  $i_*$  and  $\lambda_*$ ), and wavelength-dependent quantities:  $R_p/R_*$ ,  $q_1$ ,  $q_2$ ,  $C$ ,  $p$ , and  $\ln \sigma_{\text{infl}}$ . As in Section 3.5, each visit was normalized independently, so we included separate flux scaling parameters to absorb rotational flux variations introduced by `fleck`.

Previous long-baseline monitoring has measured rotation periods of  $11.020 \pm 0.015$  d (P. Tamburo et al. 2025)

and  $11.043^{+0.054}_{-0.053}$  d (M. Mori et al. 2025). To reduce the complex covariances between stellar orientation, rotation, and spot parameters, we imposed a cautiously wide prior of 10–12 d on  $P_{\text{rot}}$ .

Posterior sampling was performed using `pemcee` with 25 temperatures, 50 walkers, and a burn-in of 18000 steps followed by 1000 production steps. The resulting best-fit rotating spot model is shown in Figure 2. Derived spot locations are presented in Figure 3, and the spot contrasts and radii are shown in Figure 4. The joint-fit parameter inferences are summarized in the last column of Table 2.

We note that the large uncertainty inflation parameter (Table 2) for NIRISS white-lightcurves ( $\ln \sigma_{\text{NIRISS}} = 2.51$ ;  $\sigma_{\text{NIRISS}} \approx 12$ ). The NIRISS uncertainties are likely significantly underestimated as we do not account for the structured noise in the residuals (as seen in Figure 2). Future work accounting for flares, multiple spots and additional spot complexity should better model the remaining astrophysical noise in the residuals.

##### 4.3. Spectroscopic Light Curves

To extract the panchromatic spot contrast spectra, we first binned Visits 2, 4, 5, 6, and 7 to a spectral resolving power of  $R=100$ . We assumed the spot geometry ( $R_{\text{spot}}$ ,  $\phi_{\text{spot}}$ ,  $\lambda_{\text{spot}}$ ) does not vary with wavelength and adopted the white-light best-fit values for each visit (Section 4.2).

We then modeled the  $R=100$  spectroscopic light curves for each visit separately, fitting for the wavelength-dependent variables ( $R_p/R_*$ ,  $q_1$ ,  $q_2$ ,  $C$ ,  $p_0$ , and  $\ln \sigma_{\text{infl}}$ ), but now fixing the stellar orientation ( $i_*=40.8 \pm 0.3^\circ$ ,  $\lambda_*=148.9 \pm 0.4^\circ$ ), rotation period ( $P_{\text{rot}}=11.102 \pm 0.003$  d), spot radius ( $R_{\text{spot}}=0.576^{+0.006}_{-0.005} R_*$ ), and spot locations according to the joint white-light solution. Only wavelength-dependent parameters were allowed to vary. The resulting contrast spectra for all visits (except visit 1 which, though broadly consistent, has much larger errorbars due to significant masking) are displayed in Figure 5. The transmission spectrum, derived from  $R_p/R_*$ , will be presented in a future work.

#### 5. INDIVIDUAL LIGHT CURVE ANALYSIS

As a cross-check for our self-consistent joint spot model in Section 4 we also performed the same fit on each JWST visit individually. This method also allows us to quantify the potential influence of imperfect spot geometry. Although the giant polar spot appears to be long-lived (J. M. Almenara et al. 2022), the six-month separation between the GO-5863 and GO-5799 observations raises the possibility of surface evolution. Additionally, our model assumes a single circular

<sup>25</sup> <https://emcee.readthedocs.io/en/stable/tutorials/autocorr/>

Name	Parameter [Units]	Prior*	NIRSpec WLCs Only	Joint WLCs
Stellar mass	$M_* [M_\odot]$	–	$0.298^2$	$0.298^2$
Stellar rotation period	$P_{\text{rot}} [\text{d}]$	$\mathcal{U}(10, 12)$	$11.1020^3$	$11.102 \pm 0.003^1$
QLD	$(q_1, q_2)_{\text{NIRISS}}$	D. M. Kipping (2013)	–	$(0.081 \pm 0.005, 0.19 \pm 0.03)^1$
QLD	$(q_1, q_2)_{\text{NIRSpec}}$	D. M. Kipping (2013)	$(0.029 \pm 0.004, 0.017^{+0.026}_{-0.013})^1$	$(0.030 \pm 0.002, 0.04 \pm 0.03)^1$
Stellar inclination	$i_* [^\circ]$	$\mathcal{U}(0, 90)$	$25.4 \pm 0.9^1$	$40.8 \pm 0.3^1$
Sky-projected stellar obliquity	$\lambda_* [^\circ]$	$\mathcal{U}(0, 360)$	$142.3 \pm 1.2^1$	$148.9 \pm 0.4^1$
Radius ratio	$(R_p/R_*)_{\text{NIRISS}}$	$\mathcal{U}(0.1, 0.3), \mathcal{N}(0.20, 0.05)$	–	$0.18237^{+0.00011}_{-0.00012}^1$
Radius ratio	$(R_p/R_*)_{\text{NIRSpec}}$	$\mathcal{U}(0.1, 0.3), \mathcal{N}(0.20, 0.05)$	$0.18353 \pm 0.00016^1$	$0.18290 \pm 0.00008^1$
Orbital period	$P_{\text{orb}} [\text{d}]$	$\mathcal{N}(4.54, 0.10)$	$4.5445836 \pm 0.0000005^1$	4
Semi-major axis	$a/R_*$	$\mathcal{N}(25, 3)$	$24.73 \pm 0.04^1$	4
Transit epoch	$t_0 [\text{d}]$	$\mathcal{N}(60664.8947, 10 \cdot t_{\text{exp}})$	$60664.894855 \pm 0.000012^1$	4
Orbital inclination	$i [^\circ]$	$\mathcal{N}(89.7, 1.0)$	$89.54 \pm 0.02^1$	4
Eccentricity	$e$	–	$0^2$	$0^2$
Spot contrast <sup>†</sup>	$C_{\text{NIRISS}}$	$\mathcal{U}(0.0, 1.0)$	–	$0.189 \pm 0.002^1$
Spot contrast <sup>†</sup>	$C_{\text{NIRSpec}}$	$\mathcal{U}(0.0, 1.0)$	$0.1322 \pm 0.0011^1$	$0.1396^{+0.0012}_{-0.0010}^1$
Spot radius	$R_{\text{spot}} [R_*]$	$\mathcal{U}(0.0, 0.8)$	$0.480 \pm 0.004^1$	$0.576^{+0.006}_{-0.005}^1$
Spot latitude	$\phi_{\text{spot}} [^\circ]$	$\mathcal{U}(0, 90)$	$76.6 \pm 0.9^1$	$84.69 \pm 0.12^1$
Spot longitude ( $t = t_0$ )	$\lambda_{\text{spot}} [^\circ]$	$\mathcal{U}(-180, 180)$	$97.9 \pm 1.3^1$	$32.60^{+0.17}_{-0.08}^1$
Flare 1 epoch	$t_{\text{flare},1} [\text{d}]$	$\mathcal{N}(60819.407, 0.010)$	$60819.40332^{+0.00013}_{-0.00007}^1$	4
Flare 1 amplitude	$A_{\text{flare},1}$	$\mathcal{U}(0, 1)$	$0.0013^{+0.0002}_{-0.0005}^1$	4
Flare 1 FWHM	$\Delta t_{\text{flare},1} [\text{d}]$	$\mathcal{U}(0, 1)$	$0.0012 \pm 0.0004^1$	4
Flare 2 epoch	$t_{\text{flare},2} [\text{d}]$	$\mathcal{N}(60819.447, 0.010)$	$60819.4466 \pm 0.0002^1$	4
Flare 2 amplitude	$A_{\text{flare},2}$	$\mathcal{U}(0, 1)$	$0.00119 \pm 0.00008^1$	4
Flare 2 FWHM	$\Delta t_{\text{flare},2} [\text{d}]$	$\mathcal{U}(0, 1)$	$0.0075 \pm 0.0009^1$	4
Uncertainty Inflation	$\ln \sigma_{\text{NIRISS}}$	$\mathcal{U}(\ln(0.01), \ln(100))$	–	$2.51^{+0.03}_{-0.02}^1$
Uncertainty Inflation	$\ln \sigma_{\text{NIRSpec}}$	$\mathcal{U}(\ln(0.01), \ln(100))$	$0.85 \pm 0.03^1$	$0.67 \pm 0.02^1$

\*  $\mathcal{U}(A, B)$  denotes a uniform prior from  $A$  to  $B$ , and  $\mathcal{N}(A, B)$  denotes a Gaussian prior with mean  $A$  and standard deviation  $B$ .

† In this work we define contrast as:  $C = 0$  when the spot has the same temperature as the quiet photosphere and  $C = 1$  when the spot is perfectly dark ( $T = 0 \text{ K}$ ). We note that `fleck` uses the opposite definition.

[1] Derived in this work.

[2] J. E. Libby-Roberts et al. 2023

[3] P. Tamburo et al. 2025

[4] Fixed to value from NIRSpec-only fit.

**Table 2.** Derived and fixed white-light parameters for the combined three JWST/NIRSpec visits and the combined NIRSpec and NIRISS visits. For clarity all times used are in BJD TDB - 2400000.5 d. We recommend the parameters from the ‘Joint WLCs’ fit (last column) rather than the ‘NIRSpec-Only’ as the six observations cover a wider range of stellar rotation phases, placing much stronger constraints on the stellar orientation, rotation and spot properties.

spot, whereas the true morphology may consist of multiple smaller spots, non-circular structures, or regions with varying temperatures. Fitting each visit separately therefore allows us to characterize the stellar surface at each epoch without imposing constraints from stellar rotation or long-term stability.

We provide full details of the individual visit fits in Appendix C, with the resulting best-fit spot models for each visit visualized in Figure 2, locations shown in Figure 3, contrasts and radii in Figure 4, and spot contrast

spectra presented in Figure 7. Though we derive contrast spectra for each visit, we primarily perform this analysis for robustness and so we recommend readers use the results from the joint visit model (spot parameters from the last column of Table 2 and the spectrum from Figure 5).

## 6. THE POLAR SPOT SPECTRUM

From the spectroscopic fits for both the joint and individual visit models, we measure the spot contrast as a

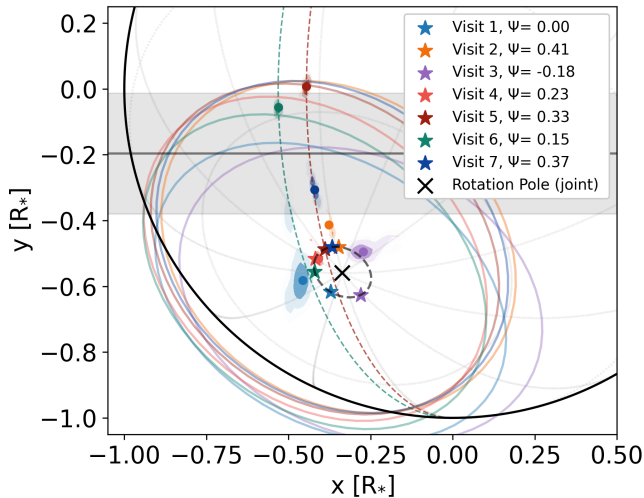


**Figure 3.** The best-fit TOI-3884 spot centers for the individual white light curve fits (solid circles with contours indicating the  $1\sigma$  and  $2\sigma$  regions from the posteriors) and the joint white light curve fit (stars). We plot ellipses indicating the extent of each spot from the self-consistent joint model. We find the best-fit solutions for Visits 5 and 6 have a spot above the transit chord (shaded grey), likely due to the geometric symmetry about the transit chord and the known radius–latitude degeneracy. Therefore, for those two visits we also include the lines of projected “longitude” along which we might expect to find degenerate spots (dotted colored lines). The black cross marks the stellar rotation pole ( $i_* = 40.8^\circ$ ,  $\lambda_* = 148.9^\circ$ ) derived in the self-consistent joint model and the dashed black line indicates how the center of the spot rotates around the pole. The stellar rotation phase,  $\Psi$ , for each visit is shown in the legend (assuming  $\Psi = 0$  at the first visit). This plot is inspired by Figure 3 from H. Chakraborty et al. (2025).

function of wavelength. The resulting spectra are shown in Figures 5 and 7.

We define spot contrast as

$$C(\lambda) = 1 - \frac{S_{\text{spot}}(T_{\text{spot}}, \log g, Z, \lambda)}{S_{\text{base}}(T_{\text{base}}, \log g, Z, \lambda)}, \quad (1)$$

where  $S_{\text{spot}}$  and  $S_{\text{base}}$  are the emergent spectra of the spotted and quiescent (baseline) photosphere, respectively, characterized by temperatures  $T_{\text{spot}}$  and  $T_{\text{base}}$ , surface gravity  $\log g$ , and metallicity,  $Z$ . We assume that  $\log g$  and  $Z$  are the same for the spot and the photosphere, although recent work has explored fitting these parameters separately (M. Fournier-Tondreau et al. 2024). Using this formalism,  $C = 0$  corresponds to a spot with the same temperature as the quiet photosphere, while  $C = 1$  represents a perfectly dark spot

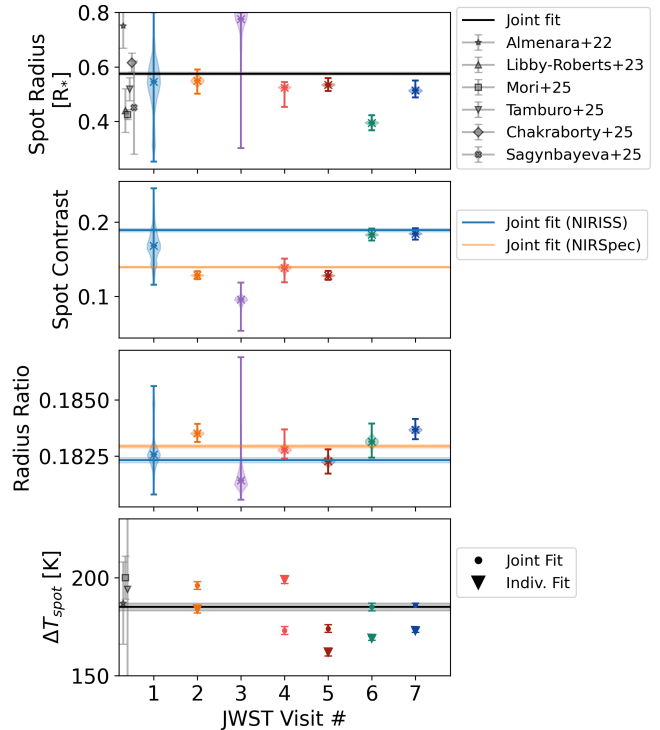


**Figure 4.** Best-fit TOI-3884 spot radii (top), instrument-dependent contrasts (upper middle) and planet-to-star radius ratios (lower middle) from each individual white light curve fit. The best-fit spot radius, contrasts, and radius ratios from the self-consistent joint model are indicated with horizontal lines. Visits 1 and 3 are significantly impacted by stellar flares, therefore are heavily masked, inflating the uncertainties of the derived parameters for these visits. The best-fit spot temperature for Visits 2, 4, 5, 6, and 7 are shown on the bottom plot.

( $T_{\text{spot}} = 0\text{K}$ ), therefore, larger temperature differences correspond to larger spot contrasts. We note that **fleck** defines spot contrast inversely such that a completely dark spot has a contrast of zero.

### 6.1. Comparison with 1D stellar models

We used `speclib`<sup>26</sup> (B. V. Rackham & J. De Wit 2024; B. V. Rackham 2023) to extract and interpolate between NewEra (P. H. Hauschildt et al. 2025) and SPHINX (A. R. Iyer et al. 2023) stellar atmosphere grids spanning  $2800 \leq T_{\text{eff}} \leq 3600\text{K}$ . Assuming the spot can be approximated as a cooler photospheric component, we also extracted NewEra/SPHINX models for temperatures cooler than the photosphere  $0 \leq \Delta T \leq 500\text{K}$ . We fixed  $\log g = 4.97$  dex and  $Z = 0.04$  following J. E. Libby-Roberts et al. (2023).

<sup>26</sup> <https://github.com/brackham/speclib>

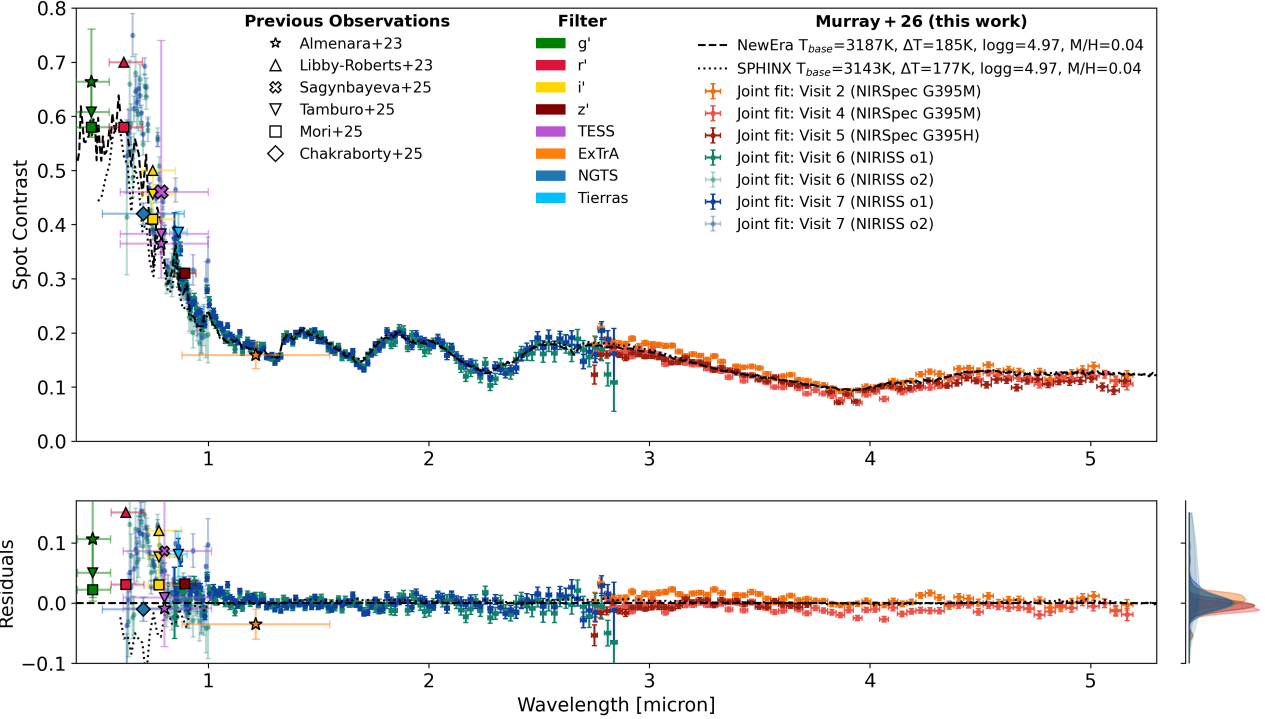


**Figure 5.** *Top:* The empirical spot contrast spectra for JWST Visits 2, 4, 5, 6, and 7. The dashed black line shows the best-fit NewEra model ( $T_{\text{base}} = 3187 \pm 15$  K,  $T_{\text{spot}} = 3002 \pm 15$  K) and dotted line shows the best-fit SPHINX model ( $T_{\text{base}} = 3143 \pm 33$  K,  $T_{\text{spot}} = 2966 \pm 34$  K). We overplot broadband contrasts derived in previous works by J. M. Almenara et al. (2022); J. E. Libby-Roberts et al. (2023); P. Tamburo et al. (2025); M. Mori et al. (2025); S. Sagynbayeva et al. (2025); H. Chakraborty et al. (2025) (compiled in Table 4). *Bottom:* Residuals between the broadband and spectroscopic contrasts and the best-fit NewEra model. A histogram of the residuals for each visit is shown to the right of the residual plot.

We fit the NewEra models to our five contrast spectra from Section 4.3, sharing  $T_{\text{base}}$ ,  $T_{\text{spot}}$ ,  $\log g$ , and  $Z$  across all visits. Because the bluer NIRISS contrasts ( $< 1 \mu\text{m}$ ) deviate significantly from the 1D model predictions (Figure 5), we restricted the fits to wavelengths longer than  $1 \mu\text{m}$ . We also fit for an uncertainty inflation parameter. Posterior sampling was performed with `emcee` using 50 walkers, 5000 burn-in steps, and 10000 production steps, verifying convergence via the auto-correlation time.

We fit the contrast spectra for two different scenarios: (a) we assume a single spot temperature across all visits, and (b) we allow the spot temperature to vary between visits. For (a) we derive  $T_{\text{base}} = 3187 \pm 15$  K and  $\Delta T_{\text{spot}} = T_{\text{base}} - T_{\text{spot}} = 185 \pm 2$  K. For (b), the results are shown in Table 3 and Figure 4. Though visit-by-visit spot temperatures vary, on average we find consistency between (a) shared and (b) independent  $\Delta T$  assumptions, and also between the individual (Section 5) and joint (Section 4) spot models.

We verified our results by repeating (a) with SPHINX models, yielding  $T_{\text{base}} = 3143 \pm 33$  K and  $\Delta T_{\text{spot}} = 177 \pm 8$  K, consistent with NewEra. Although

both models underestimate the observed spot contrasts, NewEra better reproduces the contrasts for  $\lambda \lesssim 1 \mu\text{m}$  (Figure 5; residuals up to  $\sim 15\%$  with NewEra compared to  $\sim 20\%$  with SPHINX).

In these fits we fixed the stellar metallicity and gravity. When allowed to vary, the sampling pushes against the upper prior limits of  $\log g = 6.0$  and  $Z = +0.5$ , suggesting that the 1D models attempt to compensate for mismatches in the contrast spectrum. Since fitting the contrast spectra is highly dependent on the quality of the spot fitting and the agreement with 1D stellar models, we do not consider these results reliable. Mass and radius estimates from empirical relations (A. W. Mann et al. 2015, 2019) predict  $\log g = 4.920 \pm 0.027$  dex, in line with the adopted value of  $\log g = 4.97$  dex. As J. E. Libby-Roberts et al. (2023) derived TOI-3884’s properties using high-resolution spectra from Habitable-zone Planet Finder (HPF; S. Mahadevan et al. 2012, 2014), we adopt those values here. In a future work, we will perform a full out-of-transit spectral energy distribution (SED) analysis of the JWST data to reassess the stellar

<i>(a) Shared <math>\Delta T</math></i>		
	Individual	Joint
$T_{\text{base}}$	3104±15 K	3187 ± 15 K
$\Delta T$	171±2 K	185 ± 2 K
<i>(b) Independent <math>\Delta T</math>s</i>		
$T_{\text{base}}$	3147±12 K	3172±12 K
$\Delta T_2$	184±2 K	196±2 K
$\Delta T_4$	199±2 K	173±2 K
$\Delta T_5$	162±2 K	174±2 K
$\Delta T_6$	169±1 K	185±2 K
$\Delta T_7$	173±1 K	186±1 K
$\overline{\Delta T}$	180±6 K	183±4 K

**Table 3.** Spot contrast temperatures,  $\Delta T$ , and quiescent photospheric temperatures,  $T_{\text{base}}$ , from best-fit NewEra models when (a) the spot temperature is constant across all visits, or (b) the spot temperature is independently fit for each visit.

properties and evaluate the impact of the giant polar spot on these parameters.

### 6.2. Comparison with Previous Literature

Figure 5 and Table 4 include derived broadband contrast values from a number of previous photometric TOI-3884 b studies. We find that our contrast spectrum (and extended contrast model) agrees reasonably well with the literature. Additionally, the residuals between the photometry and the best-fit NewEra model in Figure 5 appear to show a similar offset to our spectrum at bluer wavelengths ( $< 1 \mu\text{m}$ ).

Overall, our JWST-based spectrum provides the first continuous, panchromatic measurement of the polar spot contrast from 0.5–5.3  $\mu\text{m}$ , placing these broadband measurements in a unified spectral context.

## 7. DISCUSSION

TOI-3884 b is a super-Neptune planet transiting over the pole of an M dwarf that hosts a giant polar spot. By observing this unusual system with JWST and fitting the persistent spot-crossing events in transit, we derive a benchmark panchromatic spot contrast spectrum from 0.5–5.3  $\mu\text{m}$ .

### 7.1. Individual vs. Joint Visit Fits

Our individual white light curve results (see Figures 2, 3 and 4) favor a spot that is smaller and closer to the transit chord than our self-consistent joint model. For the individual fits we allow the spot to be any size and to exist anywhere on the stellar surface. For the joint model we constrain the spot properties by asserting that we have one spot (with constant radius and wavelength-dependent contrast) that is rotating about a fixed pole.

Ref.	Filter(s)	$C$
J. M. Almenara et al. (2022)	$g'$ <sup>1</sup>	0.664±0.097
	TESS <sup>2</sup>	0.365 <sup>+0.064</sup> <sub>-0.039</sub>
	ExTrA <sup>3</sup>	0.159±0.025
J. E. Libby-Roberts et al. (2023)	$r'$ <sup>1</sup>	0.5
	$i'$ <sup>1</sup>	0.5
M. Mori et al. (2025) (and private communication)	$g'$	0.58
	$r'$	0.58
	$i'$	0.41
	$z'$ <sup>1</sup>	0.31
P. Tamburo et al. (2025)	$g'$	0.608 <sup>+0.047</sup> <sub>-0.052</sub>
	$i'$	0.456 <sup>+0.043</sup> <sub>-0.044</sub>
	TESS Tierras <sup>4</sup>	0.383±0.038 0.386±0.038
H. Chakraborty et al. (2025)	NGTS <sup>5</sup>	0.42±0.02
S. Sagynbayeva et al. (2025)	TESS	0.46 <sup>+0.28</sup> <sub>-0.1</sub>

[1] The  $g'$ ,  $r'$ ,  $i'$ , and  $z'$  observations were taken with the Sloan/SDSS filters.

[2]  $\lambda = 0.6\text{--}1.0 \mu\text{m}$  with central wavelength  $\lambda_c = 0.7865 \mu\text{m}$ .

[3]  $\lambda = 0.88\text{--}1.55 \mu\text{m}$ ;  $\lambda_c = 1.215 \mu\text{m}$ .

[4]  $\lambda = 0.8235\text{--}0.9035 \mu\text{m}$ ;  $\lambda_c = 0.8635 \mu\text{m}$  (J. Garcia-Mejia et al. 2020).

[5]  $\lambda = 0.520\text{--}0.890 \mu\text{m}$ ;  $\lambda_c = 0.705 \mu\text{m}$  (P. J. Wheatley et al. 2018).

**Table 4.** Broadband spot contrast values from previous TOI-3884 b studies.

From Figure 2 we can see that the individual spot fits often describe the data better than our joint model. As we allow the spot full flexibility in the individual fits, this is to be expected when there is additional complexity beyond a single stable circular starspot. The limitations of the joint model are most evident for Visit 3, which is dominated by a flare outburst, as it does a poor job of replicating the light curve structure. Visit 3 is also the only dataset sampling the opposite half of the stellar rotation phase ( $-0.5 < \Psi < 0$ ), whereas the remaining visits lie at  $0 < \Psi < 0.5$  (Figure 3); removing it therefore weakens constraints on the global geometry in Section 4. Improving the global model will likely require additional phase coverage uncontaminated by large flares and/or more flexible spot prescriptions (e.g., multiple spots or structured active regions). Nevertheless, the agreement between the contrast spectra inferred from the individual and joint analyses (Figures 5 and 7) shows that the joint framework is sufficient for the primary goal of this work: establishing an empirical spot spectrum.

Despite differences in the spot-crossing profiles, we find consistent contrasts for the spectroscopic fits between the joint visit and individual visit models. This

reflects the fact that the contrast is primarily set by the amplitude of the spot-crossing anomaly, which is less sensitive to the radius–latitude degeneracy than the spot location itself. The largest discrepancies occur in Visits 1 and 3, where strong flare activity likely blends into the spot-crossing morphology even after masking.

Figure 7 shows the individually fit spot contrast spectra agree well at NIRISS wavelengths ( $\Delta T_{\text{spot}} = 169 \pm 1 \text{ K}$  and  $173 \pm 1 \text{ K}$  for Visits 6 and 7), but there are larger differences among the three NIRSpec visits ( $\Delta T_{\text{spot}} = 184 \pm 2 \text{ K}$ ,  $199 \pm 2 \text{ K}$ , and  $162 \pm 2 \text{ K}$  for Visits 2, 4 and 5—a 37 K range). These differences do not appear to be correlated with time, implying they are not due to evolution of the giant spot. One possible explanation is astrophysical: although the intrinsic spot doesn’t change, TOI-3884 b occults a different mixture of penumbra, umbra, and faculae at different stellar rotation phases that lead to apparent variations in the spot contrast. Alternatively, these differences may arise from the fitting process itself, as independently fitting each visit allows for slightly different solutions within the degenerate radius–latitude–contrast parameter space. Consistent with this interpretation, the self-consistent joint model reduces visit-to-visit scatter in the redder contrasts (a 23 K range; see Figure 5), implying that at least part of the variation seen in the individual fits is likely due to degeneracy-driven difficulties in the inferred spot geometry.

### 7.2. Flares

TESS photometry of TOI-3884 shows only a few definitive flares across three sectors (J. E. Libby-Roberts et al. 2023). In our JWST dataset—taken over two years later—we detect multiple small flare events, along with two large flare outbursts in Visits 1 and 3. This difference could reflect a higher activity state at the end of 2024, or it may also result from JWST’s higher precision, which enables detection of weaker flares despite the redder bandpass and decreased contrasts. Contemporaneous ground-based observations also detect flares near our JWST epochs: two flares on 11 December 2024 and 4 January 2025 with LCO (M. Mori et al. 2025), and one flare on 22 May 2025 with Tierras (P. Tamburo et al. 2025).

Notably, the two large flare outbursts in Visits 1 and 3 occur almost exactly at the same orbital phase, shortly before ingress. TOI-3884 b orbits just within the star’s Alfvén radius, where magnetic star–planet interactions (SPI) can, in principle, propagate energy back to the solar surface (S. Preusse et al. 2006; O. Cohen et al. 2011). One possibility is that the planet’s passage near the polar active region perturbs the strong magnetic field there

and triggers enhanced flare activity, consistent with SPI scenarios (E. Ilin et al. 2023, 2025; N. Whitsett & T. Daylan 2025). Long-term photometric monitoring will be needed to constrain the star’s flaring rate, and ascertain whether these events were coincidental or the result of SPI. Additionally, these processes can induce radio emission, offering an independent diagnostic (e.g., J. S. Pineda & J. Villadsen 2023; K. N. O. Ceballos et al. 2025; L. Peña-Moñino & M. Pérez-Torres 2025).

### 7.3. Spot-Modeling Limitations

Our spot modeling uses `fleck`. As noted in Section 3.3 and seen in Figure 3, `fleck` can produce “overhanging” spots near the stellar limb; if such overhang intersects the transit chord it can create bright artifacts in the light curve before or after transit. We see no (or minimal) overhang in the transit chord (Figures 2 and 3), implying negligible impact on the inferred spot-crossing shape. However, this behavior in `fleck` may still affect the likelihood landscape by disfavoring some spot solutions and potentially biasing the preferred spot position away from the mid-transit point. Reassuringly, we do note that our spot position with respect to the planet is broadly consistent by eye with analyses using different tools, including `SAGE` (H. Chakraborty et al. 2025) and `starry` (P. Tamburo et al. 2025).

As an independent check, we also compared our best-fit parameters from `fleck` with `spotter`<sup>27</sup> (L. Garcia et al. 2025), which models surface features with a pixelated stellar map. Fixing the stellar inclination and obliquity to the joint-fit values, we performed MAP optimization (without full posterior sampling) using `spotter` for five JWST visits (2, 4, 5, 6, 7) individually. We found spot radii ranging from  $0.55\text{--}0.65 R_*$ , consistent with our best-fit radius of  $0.576^{+0.006}_{-0.005} R_*$ , and with an average difference of  $0.03 R_*$  between the `spotter` and `fleck` radii. The spot latitudes from `spotter` are all  $> 77^\circ$ , with an average difference of  $5^\circ$  from `fleck` ( $84.69 \pm 0.12^\circ$ ). The `spotter` spot contrasts ( $C_{\text{NIRISS}} = 0.27$  and  $C_{\text{NIRSpec}} = 0.18$ ) are on average 0.05 larger than the `fleck` values; however, given the lack of full posterior sampling and the agreement of our contrast spectrum with previous results, we do not consider this offset significant.

Finally, our analysis neglects second-order effects from differential limb darkening across spotted versus unspotted photosphere. As this spot is both large and on the limb, such effects could be non-negligible. Quantifying them, however, likely requires detailed 3D MHD modeling (e.g., N. Kostogryz et al. 2023; N. M. Kostogryz

<sup>27</sup> <https://spotter.readthedocs.io/en/latest/>

et al. 2024) of fully convective M dwarfs like TOI-3884, which is beyond the scope of this Letter.

#### 7.4. How Well Do Models Fit the Observed Contrasts?

Despite known discrepancies between 1D models and M-dwarf spectra, our contrast spectra at wavelengths  $> 1 \mu\text{m}$  agree surprisingly well with current NewEra models. With contrast uncertainties inflated  $\times 1.9$  (the fitted inflation parameter), we find reduced chi-squared,  $\chi_r^2 = 1.6, 1.4,$  and  $1.4$  for the NIRSpec Visits 2, 4, 5 restrictively, and  $\chi_r^2 = 0.7$  and  $1.3$  for NIRISS (order 1) Visits 6 and 7 respectively. Below  $1 \mu\text{m}$ , however, we find significantly larger contrasts—up to  $\sim 15\%$ —both in the JWST spectra and in broadband photometry ( $\chi_r^2 = 2.6$  and  $5.9$  for Visits 6 and 7 with NIRISS order 2).

At these wavelengths, this may indicate missing opacities from dominant sources in M-dwarf atmospheres, such as the metal oxides TiO and VO (A. S. Rajpurohit et al. 2013; A. R. Iyer et al. 2023). These discrepancies between our spot contrast spectrum and stellar models imply that if we were to fit only optical-wavelength contrasts (without near-IR information) we would likely extract different spot and stellar properties. Numerous other works have found differences in the stellar properties derived from optical and infrared data for M dwarfs (e.g., T. Olander et al. 2021, Figure 6 from V. M. Passegger et al. 2016 and Figures 5 and 6 from D. J. Wilson et al. 2025). We also find that the size of the FeH feature at  $1 \mu\text{m}$  is underestimated by NewEra models, potentially due to difficulties modeling pressure broadening for low-mass stars (A. Glidden et al. 2026). Full interpretation of these discrepancies is beyond the scope of this Letter, but our empirical spectrum provides a direct benchmark for testing next-generation 3D MHD predictions (e.g., V. Witzke et al. 2024; H. N. Smitha et al. 2025) in future work.

We also caveat that the small uncertainties on our spot temperature ( $\pm 2\text{K}$ ) are statistical error bars from MCMC sampling, which may not fully capture the systematic uncertainties from the mismatch with stellar models, particularly at the short wavelengths we removed when fitting.

#### 7.5. Comparison with Previous TOI-3884 b Studies

Since its discovery, TOI-3884 b has been observed by many ground-based telescopes, including ExTrA (J. M. Almenara et al. 2022), APO (J. E. Libby-Roberts et al. 2023), Tierras (P. Tamburo et al. 2025), MuSCAT (M. Mori et al. 2025), and NGTS (H. Chakraborty et al. 2025). Our JWST observations extend this record by providing seven precisely measured transits over five

months, all showing a spot-crossing anomaly during the first half of transit (Figure 2). This confirms the presence of a large, stable high-latitude active region and corroborates prior reports of visit-to-visit changes in the detailed spot morphology (J. E. Libby-Roberts et al. 2023; P. Tamburo et al. 2025; M. Mori et al. 2025; H. Chakraborty et al. 2025).

By fitting six JWST visits jointly with a single rotating-spot model (Section 4), we constrain the stellar orientation and rotation period. We determine the stellar inclination to be  $i_* = 40.8 \pm 0.3^\circ$  and the sky-projected obliquity to be  $\lambda_* = 148.9 \pm 0.4^\circ$ , consistent with a misaligned orientation in which TOI-3884’s pole is directed towards us and the planet occults a high-latitude spotted region. This orientation naturally explains why the large spot-crossing signatures do not correspond to strong rotational modulation in TESS or ground-based photometry.

Long-baseline monitoring yields consistent stellar rotation periods of  $11.043^{+0.054}_{-0.053}$  d (M. Mori et al. 2025) and  $11.020 \pm 0.015$  d (P. Tamburo et al. 2025). Our rotation period estimate agrees with these results to within  $1.1\sigma$  and  $5.5\sigma$ . Though we implemented a 10–12 d prior, it is reassuring that our estimate for  $P_{\text{rot}} = 11.102 \pm 0.003$  d, derived from modeling the time-dependent shape of the spot-crossings in the light curves, aligns fairly well with independent derivations of  $P_{\text{rot}}$  from tracking the variation in TOI-3884’s brightness. Although our  $P_{\text{rot}}$  appears more precise (probably due to sharp multi-modal posterior distributions), the  $P_{\text{rot}}$  values from M. Mori et al. (2025) and P. Tamburo et al. (2025) are likely more robust, as they rely only on periodic brightness variations rather than assumptions about spot shape, stability, and multiplicity.

Using the three NIRSpec visits, we jointly constrain the orbital parameters of  $a/R_* = 24.73 \pm 0.04$ ,  $P = 4.5445836 \pm 0.0000005$  d,  $i = 89.54 \pm 0.02^\circ$ , and  $b = 0.199 \pm 0.009 R_*$ . Our  $a/R_*$  value is consistent with J. M. Almenara et al. (2022) and P. Tamburo et al. (2025) who find  $a/R_*$  values of  $25.01 \pm 0.65$  and  $25.06 \pm 0.91$ , and within  $2\sigma$  of J. E. Libby-Roberts et al. (2023)’s value of  $25.9 \pm 0.9$ . In contrast, our value is lower by  $10\sigma$  relative to H. Chakraborty et al. (2025)’s value of  $25.7 \pm 0.1$ , while all of these values are notably higher than M. Mori et al. (2025)’s value of  $23.5 \pm 0.2$ . One plausible contributor is the strong degeneracy between  $i$  and  $a/R_*$  through the transit duration, which is difficult to constrain when limb features—such as TOI-3884 b’s spot-crossing anomaly—distort ingress and egress.

Assuming a circular orbit, our results imply a stellar density of  $\rho_* = 13.85 \pm 0.07 \text{ g cm}^{-3}$ . This is consistent with  $\rho_* = 15.3 \pm 2.0 \text{ g cm}^{-3}$  from the SED/isochrone

analysis of J. E. Libby-Roberts et al. (2023). Using empirical relations (A. W. Mann et al. 2015, 2019), we also infer  $M_* = 0.282 \pm 0.006 M_\odot$  and  $R_* = 0.305 \pm 0.009 R_\odot$ , corresponding to  $\rho_* = 14.1 \pm 1.3 \text{ g cm}^{-3}$ , again consistent with our result.

From fitting the spot contrast spectrum, we find that TOI-3884’s starspot has a temperature  $185 \pm 2 \text{ K}$  cooler than the quiescent photosphere temperature of  $3187 \pm 15 \text{ K}$ . Spot temperature contrasts of order  $\sim 200 \text{ K}$  are expected for mid-M dwarfs (S. V. Berdyugina 2005), in alignment with our values. Our value of  $\Delta T$  also agrees with values derived from spot-crossings in broadband photometry (Figure 4):  $187 \pm 21 \text{ K}$  (J. M. Almenara et al. 2022),  $194 \pm 72 \text{ K}$  (P. Tamburo et al. 2025), and  $200 \pm 11 \text{ K}$  (M. Mori et al. 2025). J. E. Libby-Roberts et al. (2023) report a larger range ( $\Delta T \approx 300\text{--}500 \text{ K}$ ), while H. Chakraborty et al. (2025) and S. Sagynbayeva et al. (2025) do not quote temperatures. Agreement is strongest with studies using redder filters, consistent with the growing mismatch between empirical contrasts and 1D models at  $\lambda < 1 \mu\text{m}$ , which would drive higher inferred contrasts if interpreted through those models.

#### 7.6. The TOI-3884 Spot in Context

The TOI-3884 b system provides a rare opportunity to map a stellar active region in detail, owing to the combination of a large, long-lived polar spot and the system’s near pole-on orientation. The recurrence of a spot-crossing feature at a similar position to TESS transits, taken over two years prior, suggests that this active region persists on multi-year timescales—far exceeding the stellar rotation period. This long lifetime may reflect the reduced differential rotation expected in fully convective M dwarfs, for which lower surface temperatures and long convective-turnover timescales inhibit the shear that typically disrupts starspots (M. Küker & G. Rüdiger 2008; L. L. Kitchatinov & S. V. Olemskoy 2011).

We confirm the spot is nearly polar for TOI-3884, consistent with expectations for cool stars (M. Schuessler & S. K. Solanki 1992). Spectropolarimetric surveys (J.-F. Donati et al. 2006; C. Moutou et al. 2007; J. Morin et al. 2008, 2010) have shown that fast-rotating M dwarfs (with periods comparable to TOI-3884) can host strong, stable magnetic fields with large poloidal components, consistent with giant polar spots. Though these “polar spot caps” often have no or minimal rotational modulations that can be detected with photometry, they have been found on M dwarfs on both sides of the fully convective boundary, such as AU Mic (J. R. Barnes & A. Collier Cameron 2001; J. R. Barnes et al. 2004; B. Klein

et al. 2021) and YZ CMi (from chromatic radial velocities; D. Baroch et al. 2020).

As fully convective stars are known to have abruptly different magnetic topologies to partially-convective earlier M stars (J.-F. Donati et al. 2008; A. Reiners & G. Basri 2009), the spot spectra of TOI-3884 can help tune theoretical models of these late stellar types, making these observations synergistic to all observations of planets around cool M dwarfs.

#### 7.7. Stellar Contamination of Transmission Spectra

Our empirical spot contrasts in the NIRISS order 2 bandpass ( $\lambda=0.6\text{--}1 \mu\text{m}$ ) show poor agreement with the 1D stellar models typically used for TLS corrections. Therefore, it is possible that some signatures detected at short wavelengths on transiting planets, interpreted as Rayleigh scattering from the atmospheric gas or hazes, could be due to stellar contamination not properly corrected at short wavelengths, even when anchored well at redder wavelengths. As such, we recommend caution interpreting signals at  $\lambda < 1 \mu\text{m}$  in NIRISS transmission spectra, even if a TLS correction has been performed.

However, we find that in the NIRSpec bandpass ( $\lambda=3\text{--}5 \mu\text{m}$ ) the stellar contamination signal is smoothly varying and agrees well with 1D model expectations. This suggests that contamination is unlikely to dominate molecular detections for prominent absorbers—such as  $\text{CH}_4$ ,  $\text{CO}_2$ , or  $\text{SO}_2$ —in this wavelength range. More generally, these results highlight the advantage of NIRSpec observations in constraining planetary atmospheres in the presence of stellar activity, especially for systems with small planets transiting low-mass M dwarfs like TRAPPIST-1.

## 8. CONCLUSIONS

We have presented an analysis of seven JWST transit observations of TOI-3884 b obtained with NIRISS/SOSS and NIRSpec (G395M and G395H), spanning  $0.5\text{--}5.3 \mu\text{m}$ . These observations repeatedly capture the planet occulting a large stellar active region on its M-dwarf host star. By modeling both white-light and spectroscopic time-series data across multiple epochs, we use TOI-3884 b as a probe of the stellar surface, constraining the system geometry, the properties of the persistent polar spot, and the wavelength-dependent contrast between the spot and the surrounding photosphere. This unique dataset enables the first empirical, panchromatic ( $0.5\text{--}5.3 \mu\text{m}$ ) JWST spectrum of a starspot on an M dwarf, providing a critical empirical benchmark for stellar atmosphere models and contamination corrections.

Our main conclusions are as follows.

1. We confirm that TOI-3884 hosts a large, long-lived polar active region that is occulted in every observed transit, spanning five months. All seven JWST visits exhibit a pronounced spot-crossing anomaly in the transit light curves. While the detailed morphology of the anomaly evolves between visits, its consistent recurrence indicates that the spot structure is stable on timescales much longer than the planetary orbital period.
2. Stellar flares are frequent but do not obscure the underlying spot-crossing signal. All visits show evidence of stellar flaring to some degree, with particularly strong and complex flare activity in the earliest NIRISS observations. Despite this activity, the spot-crossing signal remains clearly detectable in every transit. While visits affected by strong flaring activity exhibit larger residuals and broader posteriors in individual fits, joint multi-visit modeling yields consistent stellar orientation and spot properties across the full dataset.
3. Repeated spot crossings tightly constrain the stellar rotation period and three-dimensional stellar orientation. By modeling the timing and morphology of repeated spot-crossing events across multiple epochs, we measure a stellar rotation period of  $P=11.102 \pm 0.003$  d and constrain the stellar inclination and sky-projected obliquity to  $i_* = 40.8 \pm 0.3^\circ$  and  $\lambda_* = 148.9 \pm 0.4^\circ$ . These results confirm that TOI-3884 is viewed nearly pole-on, naturally explaining the weak rotational modulation observed in long-term photometry despite the presence of a large spot.
4. We find the occulted spot is extremely large and located near the stellar rotation pole. Joint modeling of all visits indicates a spot radius of  $R_{\text{spot}} = 0.576^{+0.006}_{-0.005} R_*$ —over three times larger than the planet’s radius—and a latitude of  $\phi_{\text{spot}} = 84.69 \pm 0.12^\circ$ , with a projected spot-coverage fraction ranging from  $\sim 20$ – $26\%$  over the stellar rotation. Although individual visits allow some variation in inferred spot size, the spot contrast is broadly consistent across epochs, indicating that the spectral properties of the occulted region are robust to uncertainties in its detailed geometry.
5. The spot is significantly cooler than the surrounding photosphere. Comparison of the empirical contrast spectrum with 1D stellar atmosphere models indicates a spot temperature contrast of  $\Delta T = 185 \pm 2$  K relative to the photo-

sphere, corresponding to a spot temperature of  $T_{\text{spot}} = 3002 \pm 15$  K for a photospheric temperature of  $T_{\text{phot}} = 3187 \pm 15$  K.

6. The empirical spot spectrum reveals model limitations and underscores the need for direct constraints. While 1D stellar atmosphere models reproduce the observed spot contrasts reasonably well at wavelengths  $\gtrsim 1 \mu\text{m}$ , we measure significantly larger contrasts at shorter wavelengths, indicating limitations in current models and/or additional structural complexity within the active region. These discrepancies demonstrate that model-dependent contamination corrections may be incomplete, particularly in the optical. The panchromatic empirical spectrum presented here therefore provides a critical benchmark for refining stellar atmosphere models and for robustly correcting transmission spectra of planets orbiting active late-type stars.

TOI-3884 b demonstrates the power of using transiting planets as spatial probes of stellar photospheres. Extending this approach to additional JWST observations of planets transiting starspots could enable the construction of an empirical library of stellar surface spectra. Such measurements will be essential for improving stellar atmosphere models, refining contamination corrections, and ultimately enabling accurate atmospheric characterization of small planets transiting active, low-mass stars.

## 9. SOFTWARE AND THIRD PARTY DATA REPOSITORY CITATIONS

### ACKNOWLEDGMENTS

We thank Sabina Sagynbayeva for insightful conversations on parallel-tempering and `ptemcee`. We thank Mayuko Mori for sharing spot contrasts derived from their work in [M. Mori et al. \(2025\)](#).

We give thanks to the program coordinators and instrument scientist at Space Telescope, especially Michael Leveille, Glen Wahlgreen, and Tyler Baines for assisting with observation planning and scheduling for JWST-GO-5863. Based on observations with the NASA/ESA/CSA James Webb Space Telescope obtained from the Mikulski Archive for Space Telescopes (MAST) at the Space Telescope Science Institute, which is operated by the Association of Universities for Research in Astronomy, Incorporated, under NASA contract NAS5-03127. Support for program numbers JWST-GO-5863 and JWST-GO-5799 was pro-

vided through grants from the STScI under NASA contract NAS5-03127.

This material is based upon work supported by the National Aeronautics and Space Administration under Agreement No. 80NSSC21K0593 for the program “Alien Earths”. The results reported herein benefited from collaborations and/or information exchange within NASA’s Nexus for Exoplanet System Science (NExSS) research coordination network sponsored by NASA’s Science Mission Directorate. This material is based

upon work supported by the European Research Council (ERC) Synergy Grant under the European Union’s Horizon 2020 research and innovation program (grant No. 101118581—project REVEAL).

Funding for KB was provided by the European Union (ERC AdG SUBSTELLAR, GA 101054354).

*Facilities:* JWST(NIRISS, NIRSpec)

*Software:* astropy, numpy, matplotlib, emcee, ptemcee, fleck, speclib, spotter

## APPENDIX

### A. DETAILED DATA REDUCTION PROCEDURES

We reduced all seven JWST visits independently with two independent pipelines: **Eureka!** (v1.2, T. J. Bell et al. 2022)<sup>28</sup> and **ExoTEDRF** (formerly **supreme-SPOON**, M. Radica et al. 2023)<sup>29</sup>. In the main analysis, we adopt the ExoTEDRF reductions. Here we provide the detailed configuration choices and modifications applied in each pipeline.

#### A.1. *Eureka!*

**Eureka!** is an end-to-end pipeline for the reduction and analysis of JWST and HST observations (T. J. Bell et al. 2022). Its workflow is structured in six stages. The first three, which we relied upon, are dedicated to calibration, correction procedures, and optimal extraction of spectroscopic data. We analyzed the data with **Eureka!** version 1.2, which introduced support for NIRISS data reduction. Leveraging this newly added compatibility, we independently reduced both the NIRSpec and NIRISS observations. As is standard practice for NIRSpec/G395H observations, the NRS1 and NRS2 data were reduced separately. Below we describe the steps common to all reductions, and the changes made to the default **Eureka!** inputs to improve the reduction quality. We used both visual inspection of the inter-stage diagnostic outputs and the median absolute deviation value for the Stage 3 spectroscopic light curve to guide our selection of optimal reduction parameters.

Stage 1 and 2 are wrappers for the `jwst` pipeline (H. Bushouse et al. 2024, v1.18.). Stage 1 performs core detector-level processing, including ramp fitting, saturation flagging, linearity correction, dark current subtraction, and cosmic ray detection. **Eureka!** includes some targeted modifications to this stage, designed for time-series observations. These include group-level background subtraction to mitigate 1/f noise, a custom bias correction scheme for NIRSpec/G395H, and more aggressive saturation flagging. For all nine reductions we explored a variety of Stage 1 configurations. The parameters we modified from the default were: (1) the jump rejection threshold, raised from 4 to 6 $\sigma$  as commonly done for time-series observations, (2) setting the bias correction method to mean for the NIRSpec/G395H reductions, (3) enabling group level background subtraction to remove 1/f noise and adjusting the relevant background region row boundaries to [6, 160] and [3, 28] for NIRISS/SOSS and NIRSpec/G395M reductions, respectively, and (4) enabling aggressive saturation flagging for the NIRSpec/G395H observations. For Stage 2, we used the default **Eureka!** settings, performing the standard steps of world coordinate system assignment and flat field subtraction.

Prior to Stage 1, we manually corrected the NIRISS/SOSS observations for the well-known zodiacal background contamination. Rather than relying on **Eureka!**’s built-in background subtraction routines, we scaled the STScI-provided NIRISS/SOSS background model to our data, before subtracting it from each individual frame. Similarly to the ExoTEDRF reduction, the background model was scaled to match the count level of a median stack of the exposures.

Stage 3 is when **Eureka!** diverges markedly from the standard `jwst` pipeline. It produces a time-series of stellar spectra by locating the spectral trace, correcting for its curvature, performing column-by-column background subtraction via a polynomial fit with iterative sigma-clipping, and finally applying the optimal extraction algorithm of K. Horne (1986). As with Stage 1, we explore a range of configurations. Our final reductions differed from the defaults in four ways. Firstly, on a case-by-case basis, we trimmed the sub-array region of interest to retain as much of the spectral

<sup>28</sup> <https://eurekadocs.readthedocs.io/en/latest/>

<sup>29</sup> <https://exotedrf.readthedocs.io/en/latest/>

trace as possible while discarding detector regions with no signal. Secondly, we applied the full-frame outlier rejection routine along the time axis, while verifying that the fraction of flagged pixels remain well below 1%. Thirdly, we increased the outlier region threshold from  $4$  to  $6\sigma$  in the aforementioned routine. Lastly, we adjusted the background and spectral extraction aperture half-widths. For all NIRISS reduction we adopted half-widths of 27 and 24 pixels for the for the background and extraction apertures, respectively. For NIRSpec, we used apertures of 6 and 7 pixels for G395M and 8 and 9 pixels for G395H.

## A.2. *ExoTEDRF*

We perform a second, independent reduction using the EXOplanet Transit and Eclipse Data Reduction Framework! (*ExoTEDRF*; A. D. Feinstein et al. 2023; M. Radica et al. 2023; M. Radica 2024). Similarly to *Eureka!*, *ExoTEDRF* provides an end-to-end reduction and analysis pipeline for JWST exoplanet time series observations. *ExoTEDRF* was initially optimized for NIRISS/SOSS; however it now supports reduction techniques for NIRSpec/BOTS as well. Thus, we used *ExoTEDRF* to independently reduce all NIRISS/SOSS and NIRSpec/G395M/G395H observations. We describe our NIRISS/SOSS reduction, followed by NIRSpec.

### A.2.1. *NIRISS/SOSS*

We performed Stage 1 corrections on our NIRISS/SOSS observations using the *jwst* pipeline with additional modifications. Stage 1 corrections that used the *jwst* pipeline include initializing the data quality flags and saturated pixel flags, superbias subtraction, reference pixel correction, dark current correction, and background correction. We correct the background by scaling the NIRISS/SOSS background model provided by STScI to our observations. This scaling is determined by scaling the model background to the counts level of a median stack of the exposures. There are very few regions of the exposure that are not illuminated by the SOSS point spread function. For these observations, we use the following region:  $x = [230, 250]$ ;  $y = [350, 550]$ , as is standard within *ExoTEDRF*. After this stage, we perform  $1/f$  noise correction at the group level, as group-level correction can lead to higher precision light curves with lower noise levels (A. Carter et al. 2025). We use the “scale-achromatic”  $1/f$  noise correction within *ExoTEDRF*, which constructs difference images of each exposure by subtracting a median image, then subtracts the median value from each column. The scaled background is then re-added to the exposures, as it needs to be flat field corrected. The remaining Stage 1 steps are standard with the *jwst* pipeline.

For our Stage 2 processing, we again apply the standard *jwst* pipeline routines of assigning the world coordinate system and flat field subtraction. Here, we subtract the scaled STScI background model, which was described in the Stage 1 processing. We then correct for bad pixels and run the principal component analysis reconstruction step (M. Radica et al. 2025). This stage allows us to remove similar components between exposures, such as components which correspond to detector systematics. We extract our stellar spectra using a standard box extraction with an aperture width of 30 pixels.

### A.2.2. *NIRSpec/BOTS*

Our NIRSpec/G395M/G395H reduction is nearly identical to our NIRISS/SOSS reduction, with some modifications. First, we do not need to correct for the same structured background that is seen in NIRISS/SOSS. Second, in our Stage 2 processing, we perform wavelength correction in the instance the target is not perfectly centered in the slit. Third, we perform additional  $1/f$  noise correction at the integration level. This removes any potential residual noise that may still be present, even after the aforementioned reduction steps. Again, we extract our stellar spectra using a standard box extraction with an aperture width of 8 pixels. This was performed independently for NIRSpec/G395H NRS1 and NRS2 detectors.

## B. FLARE OUTBURST EVENTS

Here we illustrate the large flare outburst events observed during the early JWST visits. Figure 6 compares the NIRISS order 2 white light curves to light curves extracted around  $H\alpha$ , highlighting the chromospheric origin and temporal structure of these events.

## C. DETAILS OF THE INDIVIDUAL LIGHT CURVE ANALYSIS

To verify our results from Section 4 we performed a similar light curve analysis on each JWST visit individually. In this appendix we describe the details of the white light and spectroscopic light curve fits. In this analysis we opted

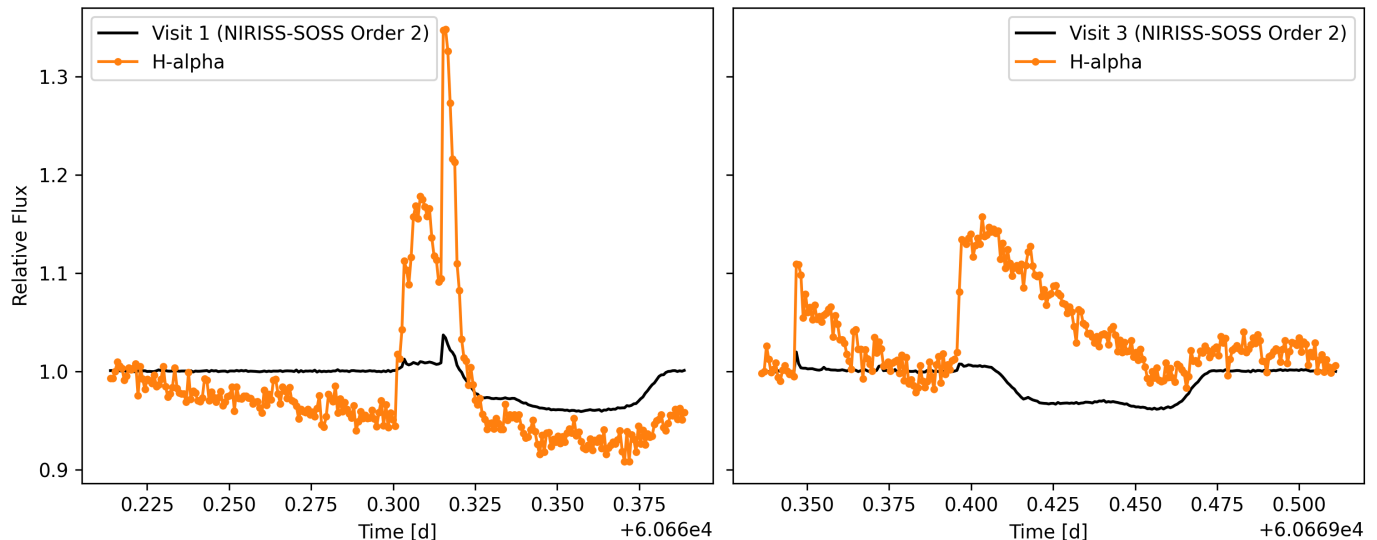


**Figure 6.** White light curves from the JWST-GO-5863 observations of TOI-3884 b, taken with NIRISS/SOSS (order 2, 0.63–1.10  $\mu\text{m}$ ), shown in black. Light curves extracted around H $\alpha$  emission (0.655–0.6565  $\mu\text{m}$ ) are overplotted in orange.

to include Visits 1 and 3, but mask the obvious flaring regions (Figure 2), leaving partial transits and spot-crossings to fit. When we fit Visit 3 (rather than removing as in Section 4), we find discrepant  $R_{\text{spot}}$  and  $C$  values (Figure 4), further justifying our decision to remove the visit from our joint analysis.

### C.1. White-Light Fits

For each of the seven white light curves (Order 1 for NIRISS and NRS1 for NIRSpec/G395H), we fixed the wavelength-independent stellar and planetary parameters to the results from the NIRSpec joint fit (Table 2), while allowing the spot to vary. Therefore, we fit only for the spot parameters ( $R_{\text{spot}}$ ,  $\phi_{\text{spot}}$  and  $\lambda_{\text{spot}}$ ) and wavelength-dependent quantities:  $R_p/R_*$ ,  $q_1$ ,  $q_2$ ,  $C$ ,  $p$ , and  $\ln \sigma_{\text{inff}}$ . The parameter posteriors were sampled with `ptemcee` as in Section 3.5, but with 25 temperatures, 30 walkers, and a burn-in of 5000 steps followed by 10000 steps. In all cases, chain lengths exceeded the integrated autocorrelation time, indicating convergence.

### C.2. Spectroscopic Light Curves

Similarly to Section 4.3, we fit each of the  $R=100$  light curves, adopting the white-light best-fit values for each visit from Section C.1. We opted not to include Visits 1 and 3 due to lack of constraint on spot radius and contrast (Figure 4). As in Section 4.3, we fitted only for the wavelength-dependent variables and flare amplitudes in Visit 5. The  $R=100$  spot contrast spectra for each visit are displayed in Figure 7.

## REFERENCES

- Allen, N. H., Espinoza, N., Boehm, V. A., et al. 2026, *AJ*, 171, 105, doi: [10.3847/1538-3881/ae28cb](https://doi.org/10.3847/1538-3881/ae28cb)
- Almenara, J. M., Bonfils, X., Forveille, T., et al. 2022, *Astronomy & Astrophysics*, 667, L11, doi: [10.1051/0004-6361/202244791](https://doi.org/10.1051/0004-6361/202244791)
- Barclay, T., Sheppard, K. B., Latouf, N., et al. 2025, *The Astronomical Journal*, 169, 241, doi: [10.3847/1538-3881/ada5f6](https://doi.org/10.3847/1538-3881/ada5f6)
- Barnes, J. R., & Collier Cameron, A. 2001, *MNRAS*, 326, 950, doi: [10.1046/j.1365-8711.2001.04649.x](https://doi.org/10.1046/j.1365-8711.2001.04649.x)
- Barnes, J. R., James, D. J., & Collier Cameron, A. 2004, *MNRAS*, 352, 589, doi: [10.1111/j.1365-2966.2004.07949.x](https://doi.org/10.1111/j.1365-2966.2004.07949.x)
- Baroch, D., Morales, J. C., Ribas, I., et al. 2020, *Astronomy & Astrophysics*, 641, A69, doi: [10.1051/0004-6361/202038213](https://doi.org/10.1051/0004-6361/202038213)
- Bell, T. J., Ahrer, E.-M., Brande, J., et al. 2022, *Journal of Open Source Software*, 7, 4503, doi: [10.21105/joss.04503](https://doi.org/10.21105/joss.04503)
- Berdugina, S. V. 2005, *Living Reviews in Solar Physics*, 2, 8, doi: [10.12942/lrsp-2005-8](https://doi.org/10.12942/lrsp-2005-8)
- Burn, R., Schlecker, M., Mordasini, C., et al. 2021, *Astronomy and Astrophysics*, 656, A72, doi: [10.1051/0004-6361/202140390](https://doi.org/10.1051/0004-6361/202140390)

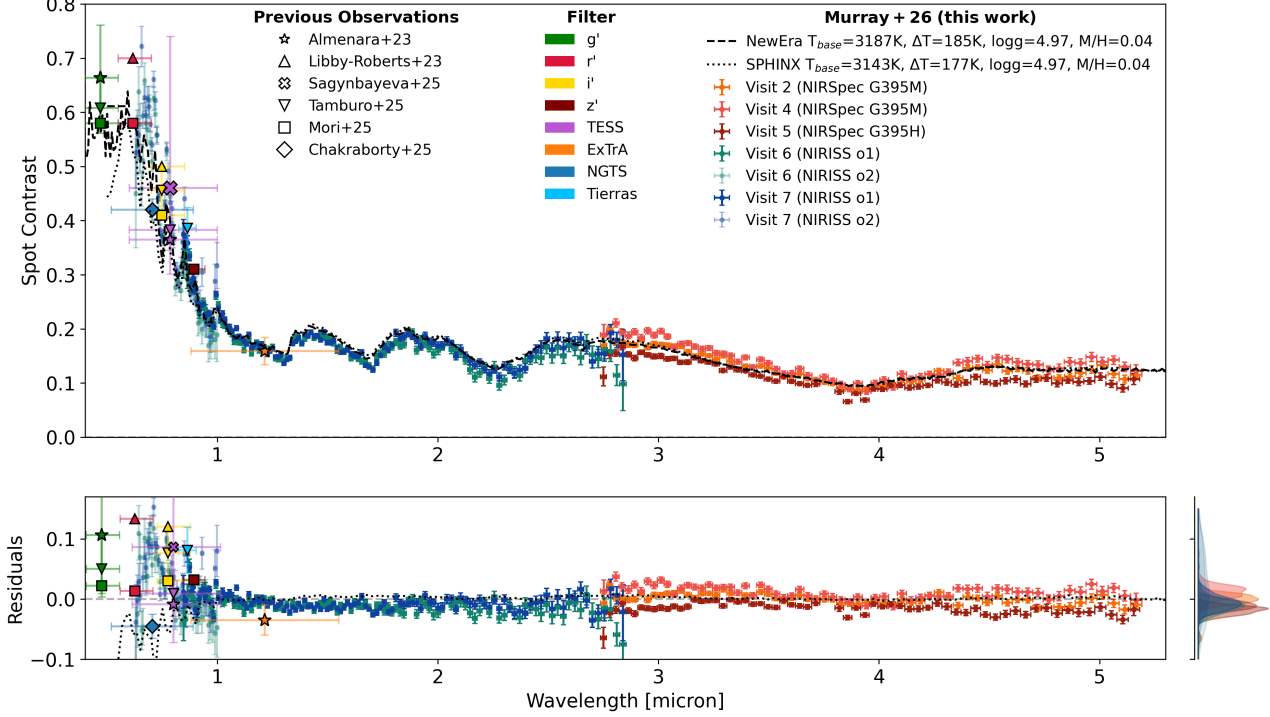


**Figure 7.** Similar to Figure 5, but for the individually fit light curves described in Sections 5 and C. The best-fit NewEra/SPHINX models for the self-consistent joint model are overplotted in black.

Bushouse, H., Eisenhamer, J., Dencheva, N., et al. 2024, JWST Calibration Pipeline, Zenodo, doi: [10.5281/ZENODO.10870758](https://doi.org/10.5281/ZENODO.10870758)

Cadieux, C., Doyon, R., MacDonald, R. J., et al. 2024, The Astrophysical Journal, 970, L2, doi: [10.3847/2041-8213/ad5afa](https://doi.org/10.3847/2041-8213/ad5afa)

Carter, A., Espinoza, N., Albert, L., et al. 2025, Effects of Jump Detection and Ramp Fitting Algorithms on NIRISS/SOSS Exoplanet Time-Series Observations, arXiv, doi: [10.48550/ARXIV.2505.05571](https://doi.org/10.48550/ARXIV.2505.05571)

Ceballos, K. N. O., Cendes, Y., & Berger, E. 2025, A Radio Search for Star-Planet Interaction in TOI-540 and SPECULOOS-3, arXiv, doi: [10.48550/ARXIV.2512.16852](https://doi.org/10.48550/ARXIV.2512.16852)

Chabrier, G., & Baraffe, I. 1997, Astronomy and Astrophysics, 327, 1039, doi: [10.48550/arXiv.astro-ph/9704118](https://doi.org/10.48550/arXiv.astro-ph/9704118)

Chakraborty, H., Almenara, J. M., Lendl, M., et al. 2025, Astronomy & Astrophysics, 702, A100, doi: [10.1051/0004-6361/202555998](https://doi.org/10.1051/0004-6361/202555998)

Cohen, O., Kashyap, V. L., Drake, J. J., et al. 2011, The Astrophysical Journal, 733, 67, doi: [10.1088/0004-637X/733/1/67](https://doi.org/10.1088/0004-637X/733/1/67)

Davoudi, F., Rackham, B. V., Gillon, M., et al. 2024, ApJL, 970, L4, doi: [10.3847/2041-8213/ad5c6c](https://doi.org/10.3847/2041-8213/ad5c6c)

de Wit, J., Wakeford, H. R., Gillon, M., et al. 2016, Nature, 537, 69, doi: [10.1038/nature18641](https://doi.org/10.1038/nature18641)

de Wit, J., Wakeford, H. R., Lewis, N. K., et al. 2018, Nature Astronomy, 2, 214, doi: [10.1038/s41550-017-0374-z](https://doi.org/10.1038/s41550-017-0374-z)

Donati, J.-F., Forveille, T., Cameron, A. C., et al. 2006, Science, 311, 633, doi: [10.1126/science.1121102](https://doi.org/10.1126/science.1121102)

Donati, J.-F., Morin, J., Petit, P., et al. 2008, Monthly Notices of the Royal Astronomical Society, 390, 545, doi: [10.1111/j.1365-2966.2008.13799.x](https://doi.org/10.1111/j.1365-2966.2008.13799.x)

Doyon, R., Willott, C. J., Hutchings, J. B., et al. 2023, PASP, 135, 098001, doi: [10.1088/1538-3873/acd41b](https://doi.org/10.1088/1538-3873/acd41b)

Dunkley, J., Bucher, M., Ferreira, P. G., Moodley, K., & Skordis, C. 2005, Monthly Notices of the Royal Astronomical Society, 356, 925, doi: [10.1111/j.1365-2966.2004.08464.x](https://doi.org/10.1111/j.1365-2966.2004.08464.x)

Earl, D. J., & Deem, M. W. 2005, Physical Chemistry Chemical Physics, 7, 3910, doi: [10.1039/b509983h](https://doi.org/10.1039/b509983h)

Espinoza, N., Rackham, B. V., Jordán, A., et al. 2019, Monthly Notices of the Royal Astronomical Society, 482, 2065, doi: [10.1093/mnras/sty2691](https://doi.org/10.1093/mnras/sty2691)

Espinoza, N., Allen, N. H., Glidden, A., et al. 2025, ApJL, 990, L52, doi: [10.3847/2041-8213/adf42e](https://doi.org/10.3847/2041-8213/adf42e)

Feinstein, A. D., Radica, M., Welbanks, L., et al. 2023, Nature, 614, 670, doi: [10.1038/s41586-022-05674-1](https://doi.org/10.1038/s41586-022-05674-1)

- Feinstein, A. D., Radica, M., Welbanks, L., et al. 2023, *Nature*, 614, 670, doi: [10.1038/s41586-022-05674-1](https://doi.org/10.1038/s41586-022-05674-1)
- Foreman-Mackey, D., Hogg, D. W., Lang, D., & Goodman, J. 2013, *Publications of the Astronomical Society of the Pacific*, 125, 306, doi: [10.1086/670067](https://doi.org/10.1086/670067)
- Fournier-Tondreau, M., MacDonald, R. J., Radica, M., et al. 2024, *Monthly Notices of the Royal Astronomical Society*, 528, 3354, doi: [10.1093/mnras/stad3813](https://doi.org/10.1093/mnras/stad3813)
- Garcia, L., Rackham, B. V., & Panwar, V. 2025, *Journal of Open Source Software*, 10, 8305, doi: [10.21105/joss.08305](https://doi.org/10.21105/joss.08305)
- Garcia, L. J., Moran, S. E., Rackham, B. V., et al. 2022, *Astronomy and Astrophysics*, 665, A19, doi: [10.1051/0004-6361/202142603](https://doi.org/10.1051/0004-6361/202142603)
- Garcia-Mejia, J., Charbonneau, D. B., Fabricant, D. G., et al. 2020, in *Ground-based and Airborne Telescopes VIII*, ed. H. K. Marshall, J. Spyromilio, & T. Usuda (Online Only, United States: SPIE), 168, doi: [10.1117/12.2561467](https://doi.org/10.1117/12.2561467)
- Gardner, J. P., Mather, J. C., Clampin, M., et al. 2006, *Space Science Reviews*, 123, 485, doi: [10.1007/s11214-006-8315-7](https://doi.org/10.1007/s11214-006-8315-7)
- Geyer, C. J. 1991, in *Computing science and statistics : proceedings of the 23rd Symposium on the Interface*, Seattle, Washington. <https://api.semanticscholar.org/CorpusID:60236374>
- Glidden, A., Witzke, V., Shapiro, A. I., & Seager, S. 2026, *The Astrophysical Journal Letters*, 997, L8, doi: [10.3847/2041-8213/ae3137](https://doi.org/10.3847/2041-8213/ae3137)
- Glidden, A., Ranjan, S., Seager, S., et al. 2025, *ApJL*, 990, L53, doi: [10.3847/2041-8213/adf62e](https://doi.org/10.3847/2041-8213/adf62e)
- Hauschildt, P. H., Barman, T., Baron, E., Aufdenberg, J. P., & Schweitzer, A. 2025, *Astronomy & Astrophysics*, 698, A47, doi: [10.1051/0004-6361/202554171](https://doi.org/10.1051/0004-6361/202554171)
- Hogg, D. W., & Foreman-Mackey, D. 2018, *The Astrophysical Journal Supplement Series*, 236, 11, doi: [10.3847/1538-4365/aab76e](https://doi.org/10.3847/1538-4365/aab76e)
- Horne, K. 1986, *PASP*, 98, 609, doi: [10.1086/131801](https://doi.org/10.1086/131801)
- Huber, K. F., Czesla, S., Wolter, U., & Schmitt, J. H. M. M. 2010, *Astronomy & Astrophysics*, 514, A39, doi: [10.1051/0004-6361/200913914](https://doi.org/10.1051/0004-6361/200913914)
- Husser, T. O., Wende-von Berg, S., Dreizler, S., et al. 2013, *Astronomy and Astrophysics*, 553, A6, doi: [10.1051/0004-6361/201219058](https://doi.org/10.1051/0004-6361/201219058)
- Ida, S., & Lin, D. N. C. 2005, *The Astrophysical Journal*, 626, 1045, doi: [10.1086/429953](https://doi.org/10.1086/429953)
- Ilin, E., Poppenhäger, K., Chebly, J., Ilić, N., & Alvarado-Gómez, J. D. 2023, *Monthly Notices of the Royal Astronomical Society*, 527, 3395, doi: [10.1093/mnras/stad3398](https://doi.org/10.1093/mnras/stad3398)
- Ilin, E., Vedantham, H. K., Poppenhäger, K., et al. 2025, *Nature*, 643, 645, doi: [10.1038/s41586-025-09236-z](https://doi.org/10.1038/s41586-025-09236-z)
- Iyer, A. R., & Line, M. R. 2020, *The Astrophysical Journal*, 889, 78, doi: [10.3847/1538-4357/ab612e](https://doi.org/10.3847/1538-4357/ab612e)
- Iyer, A. R., Line, M. R., Muirhead, P. S., Fortney, J. J., & Gharib-Nezhad, E. 2023, *The Astrophysical Journal*, 944, 41, doi: [10.3847/1538-4357/acabc2](https://doi.org/10.3847/1538-4357/acabc2)
- Jakobsen, P., Ferruit, P., Alves de Oliveira, C., et al. 2022, *A&A*, 661, A80, doi: [10.1051/0004-6361/202142663](https://doi.org/10.1051/0004-6361/202142663)
- Kipping, D. M. 2013, *Monthly Notices of the Royal Astronomical Society*, 435, 2152, doi: [10.1093/mnras/stt1435](https://doi.org/10.1093/mnras/stt1435)
- Kitchatinov, L. L., & Olemskoy, S. V. 2011, *Monthly Notices of the Royal Astronomical Society*, 411, 1059, doi: [10.1111/j.1365-2966.2010.17737.x](https://doi.org/10.1111/j.1365-2966.2010.17737.x)
- Klein, B., Donati, J.-F., Moutou, C., et al. 2021, *MNRAS*, 502, 188, doi: [10.1093/mnras/staa3702](https://doi.org/10.1093/mnras/staa3702)
- Kostogryz, N., Shapiro, A. I., Witzke, V., et al. 2023, *Research Notes of the AAS*, 7, 39, doi: [10.3847/2515-5172/acc180](https://doi.org/10.3847/2515-5172/acc180)
- Kostogryz, N. M., Shapiro, A. I., Witzke, V., et al. 2024, *Nature Astronomy*, 8, 929, doi: [10.1038/s41550-024-02252-5](https://doi.org/10.1038/s41550-024-02252-5)
- Kreidberg, L. 2015, *Publications of the Astronomical Society of the Pacific*, 127, 1161, doi: [10.1086/683602](https://doi.org/10.1086/683602)
- Küker, M., & Rüdiger, G. 2008, *Journal of Physics: Conference Series*, 118, 012029, doi: [10.1088/1742-6596/118/1/012029](https://doi.org/10.1088/1742-6596/118/1/012029)
- Laughlin, G., Bodenheimer, P., & Adams, F. C. 2004, *The Astrophysical Journal*, 612, L73, doi: [10.1086/424384](https://doi.org/10.1086/424384)
- Libby-Roberts, J. E., Schutte, M., Hebb, L., et al. 2023, *The Astronomical Journal*, 165, 249, doi: [10.3847/1538-3881/accc2f](https://doi.org/10.3847/1538-3881/accc2f)
- Lim, O., Benneke, B., Doyon, R., et al. 2023, *The Astrophysical Journal*, 955, L22, doi: [10.3847/2041-8213/acf7c4](https://doi.org/10.3847/2041-8213/acf7c4)
- Mahadevan, S., Ramsey, L., Bender, C., et al. 2012, in *SPIE Astronomical Telescopes + Instrumentation*, ed. I. S. McLean, S. K. Ramsay, & H. Takami, Amsterdam, Netherlands, 84461S, doi: [10.1117/12.926102](https://doi.org/10.1117/12.926102)
- Mahadevan, S., Ramsey, L. W., Terrien, R., et al. 2014, in *SPIE Astronomical Telescopes + Instrumentation*, ed. S. K. Ramsay, I. S. McLean, & H. Takami, Montréal, Quebec, Canada, 91471G, doi: [10.1117/12.2056417](https://doi.org/10.1117/12.2056417)
- Mancini, L., Southworth, J., Raia, G., et al. 2017, *Monthly Notices of the Royal Astronomical Society*, 465, 843, doi: [10.1093/mnras/stw1987](https://doi.org/10.1093/mnras/stw1987)
- Mann, A. W., Feiden, G. A., Gaidos, E., Boyajian, T., & Braun, K. V. 2015, *The Astrophysical Journal*, 804, 64, doi: [10.1088/0004-637X/804/1/64](https://doi.org/10.1088/0004-637X/804/1/64)

- Mann, A. W., Dupuy, T., Kraus, A. L., et al. 2019, *The Astrophysical Journal*, 871, 63, doi: [10.3847/1538-4357/aaf3bc](https://doi.org/10.3847/1538-4357/aaf3bc)
- May, E. M., MacDonald, R. J., Bennett, K. A., et al. 2023, *Double Trouble: Two Transits of the Super-Earth GJ 1132 b Observed with JWST NIRSpec G395H*, arXiv. <http://arxiv.org/abs/2310.10711>
- Mendoza, G. T., Davenport, J. R. A., Agol, E., Jackman, J. A. G., & Hawley, S. L. 2022, *The Astronomical Journal*, 164, 17, doi: [10.3847/1538-3881/ac6fe6](https://doi.org/10.3847/1538-3881/ac6fe6)
- Mikal-Evans, T., Madhusudhan, N., Dittmann, J., et al. 2023, *The Astronomical Journal*, 165, 84, doi: [10.3847/1538-3881/aca90b](https://doi.org/10.3847/1538-3881/aca90b)
- Morales, J. C., Mustill, A. J., Ribas, I., et al. 2019, *Science*, 365, 1441, doi: [10.1126/science.aax3198](https://doi.org/10.1126/science.aax3198)
- Moran, S. E., Stevenson, K. B., Sing, D. K., et al. 2023, *The Astrophysical Journal*, 948, L11, doi: [10.3847/2041-8213/acb9c](https://doi.org/10.3847/2041-8213/acb9c)
- Mori, M., Fukui, A., Hirano, T., et al. 2025, *The Astronomical Journal*, 170, 204, doi: [10.3847/1538-3881/ade2df](https://doi.org/10.3847/1538-3881/ade2df)
- Morin, J., Donati, J.-F., Petit, P., et al. 2010, *Monthly Notices of the Royal Astronomical Society*, 407, 2269, doi: [10.1111/j.1365-2966.2010.17101.x](https://doi.org/10.1111/j.1365-2966.2010.17101.x)
- Morin, J., Donati, J. F., Petit, P., et al. 2008, *Monthly Notices of the Royal Astronomical Society*, 390, 567, doi: [10.1111/j.1365-2966.2008.13809.x](https://doi.org/10.1111/j.1365-2966.2008.13809.x)
- Morris, B. 2020, *Journal of Open Source Software*, 5, 2103, doi: [10.21105/joss.02103](https://doi.org/10.21105/joss.02103)
- Morris, B. M., Hebb, L., Davenport, J. R. A., Rohn, G., & Hawley, S. L. 2017, *The Astrophysical Journal*, 846, 99, doi: [10.3847/1538-4357/aa8555](https://doi.org/10.3847/1538-4357/aa8555)
- Moutou, C., Donati, J.-F., Savalle, R., et al. 2007, *A&A*, 473, 651, doi: [10.1051/0004-6361:20077795](https://doi.org/10.1051/0004-6361:20077795)
- Newton, E. R., Irwin, J., Charbonneau, D., et al. 2017, *ApJ*, 834, 85, doi: [10.3847/1538-4357/834/1/85](https://doi.org/10.3847/1538-4357/834/1/85)
- Newton, E. R., Irwin, J., Charbonneau, D., et al. 2016, *ApJ*, 821, 93, doi: [10.3847/0004-637X/821/2/93](https://doi.org/10.3847/0004-637X/821/2/93)
- Olander, T., Heiter, U., & Kochukhov, O. 2021, *Astronomy & Astrophysics*, 649, A103, doi: [10.1051/0004-6361/202039747](https://doi.org/10.1051/0004-6361/202039747)
- Pasegger, V. M., Wende-von Berg, S., & Reiners, A. 2016, *Astronomy & Astrophysics*, 587, A19, doi: [10.1051/0004-6361/201322261](https://doi.org/10.1051/0004-6361/201322261)
- Peña-Moñino, L., & Pérez-Torres, M. 2025, *Monthly Notices of the Royal Astronomical Society*, 544, 1220, doi: [10.1093/mnras/staf1467](https://doi.org/10.1093/mnras/staf1467)
- Piaulet-Ghorayeb, C., Benneke, B., Turbet, M., et al. 2025, *The Astrophysical Journal*, 989, 181, doi: [10.3847/1538-4357/adf207](https://doi.org/10.3847/1538-4357/adf207)
- Pineda, J. S., & Villadsen, J. 2023, *Nature Astronomy*, 7, 569, doi: [10.1038/s41550-023-01914-0](https://doi.org/10.1038/s41550-023-01914-0)
- Pont, F., Sing, D. K., Gibson, N. P., et al. 2013, *Monthly Notices of the Royal Astronomical Society*, 432, 2917, doi: [10.1093/mnras/stt651](https://doi.org/10.1093/mnras/stt651)
- Preusse, S., Kopp, A., Büchner, J., & Motschmann, U. 2006, *Astronomy & Astrophysics*, 460, 317, doi: [10.1051/0004-6361:20065353](https://doi.org/10.1051/0004-6361:20065353)
- Rackham, B., Espinoza, N., Apai, D., et al. 2017, *The Astrophysical Journal*, 834, 151, doi: [10.3847/1538-4357/aa4f6c](https://doi.org/10.3847/1538-4357/aa4f6c)
- Rackham, B. V. 2023, *speclib*, Zenodo, doi: [10.5281/ZENODO.7868050](https://doi.org/10.5281/ZENODO.7868050)
- Rackham, B. V., Apai, D., & Giampapa, M. S. 2018, *The Astrophysical Journal*, 853, 122, doi: [10.3847/1538-4357/aaa08c](https://doi.org/10.3847/1538-4357/aaa08c)
- Rackham, B. V., Apai, D., & Giampapa, M. S. 2019, *The Astronomical Journal*, 157, 96, doi: [10.3847/1538-3881/aaf892](https://doi.org/10.3847/1538-3881/aaf892)
- Rackham, B. V., & De Wit, J. 2024, *The Astronomical Journal*, 168, 82, doi: [10.3847/1538-3881/ad5833](https://doi.org/10.3847/1538-3881/ad5833)
- Rackham, B. V., Espinoza, N., Berdyugina, S. V., et al. 2023, *RAS Techniques and Instruments*, 2, 148, doi: [10.1093/rasti/rzad009](https://doi.org/10.1093/rasti/rzad009)
- Radica, M. 2024, *The Journal of Open Source Software*, 9, 6898, doi: [10.21105/joss.06898](https://doi.org/10.21105/joss.06898)
- Radica, M. 2024, *Journal of Open Source Software*, 9, 6898, doi: [10.21105/joss.06898](https://doi.org/10.21105/joss.06898)
- Radica, M., Welbanks, L., Espinoza, N., et al. 2023, *Monthly Notices of the Royal Astronomical Society*, 524, 835, doi: [10.1093/mnras/stad1762](https://doi.org/10.1093/mnras/stad1762)
- Radica, M., Piaulet-Ghorayeb, C., Taylor, J., et al. 2025, *The Astrophysical Journal Letters*, 979, L5, doi: [10.3847/2041-8213/ada381](https://doi.org/10.3847/2041-8213/ada381)
- Rajpurohit, A. S., Reylé, C., Allard, F., et al. 2013, *Astronomy & Astrophysics*, 556, A15, doi: [10.1051/0004-6361/201321346](https://doi.org/10.1051/0004-6361/201321346)
- Rathcke, A. D., Buchhave, L. A., de Wit, J., et al. 2025, *ApJL*, 979, L19, doi: [10.3847/2041-8213/ada5c7](https://doi.org/10.3847/2041-8213/ada5c7)
- Reiners, A., & Basri, G. 2009, *Astronomy & Astrophysics*, 496, 787, doi: [10.1051/0004-6361:200811450](https://doi.org/10.1051/0004-6361:200811450)
- Sagynbayeva, S., Farr, W. M., Morris, B. M., & Luger, R. 2025, *The Astrophysical Journal*, 990, 32, doi: [10.3847/1538-4357/adf6be](https://doi.org/10.3847/1538-4357/adf6be)
- Schuessler, M., & Solanki, S. K. 1992, *Astronomy and Astrophysics*, 264, L13. <https://ui.adsabs.harvard.edu/abs/1992A&A...264L..13S>
- Sing, D. K., Pont, F., Aigrain, S., et al. 2011, *Monthly Notices of the Royal Astronomical Society*, 416, 1443, doi: [10.1111/j.1365-2966.2011.19142.x](https://doi.org/10.1111/j.1365-2966.2011.19142.x)

- Smitha, H. N., Shapiro, A. I., Witzke, V., et al. 2025, *The Astrophysical Journal Letters*, 978, L13, doi: [10.3847/2041-8213/ad9aaa](https://doi.org/10.3847/2041-8213/ad9aaa)
- Swendsen, R. H., & Wang, J.-S. 1986, *Physical Review Letters*, 57, 2607, doi: [10.1103/PhysRevLett.57.2607](https://doi.org/10.1103/PhysRevLett.57.2607)
- Tamburo, P., Yee, S. W., García-Mejía, J., et al. 2025, *The Astronomical Journal*, 170, 200, doi: [10.3847/1538-3881/adf72f](https://doi.org/10.3847/1538-3881/adf72f)
- Vousden, W. D., Farr, W. M., & Mandel, I. 2016, *Monthly Notices of the Royal Astronomical Society*, 455, 1919, doi: [10.1093/mnras/stv2422](https://doi.org/10.1093/mnras/stv2422)
- Wakeford, H. R., Lewis, N. K., Fowler, J., et al. 2019, *The Astronomical Journal*, 157, 11, doi: [10.3847/1538-3881/aaf04d](https://doi.org/10.3847/1538-3881/aaf04d)
- Wheatley, P. J., West, R. G., Goad, M. R., et al. 2018, *Monthly Notices of the Royal Astronomical Society*, 475, 4476, doi: [10.1093/mnras/stx2836](https://doi.org/10.1093/mnras/stx2836)
- Whitsett, N., & Daylan, T. 2025, *Induced-Flare Candidates from the TESS Mission*, arXiv, doi: [10.48550/ARXIV.2509.22918](https://doi.org/10.48550/ARXIV.2509.22918)
- Wilson, D. J., Froning, C. S., Duvvuri, G. M., et al. 2025, *The Astrophysical Journal*, 978, 85, doi: [10.3847/1538-4357/ad9251](https://doi.org/10.3847/1538-4357/ad9251)
- Witzke, V., Shapiro, A. I., Kostogryz, N. M., et al. 2024, *Astronomy & Astrophysics*, 681, A81, doi: [10.1051/0004-6361/202346099](https://doi.org/10.1051/0004-6361/202346099)
- Zhang, Z., Zhou, Y., Rackham, B. V., & Apai, D. 2018, *The Astronomical Journal*, 156, 178, doi: [10.3847/1538-3881/aade4f](https://doi.org/10.3847/1538-3881/aade4f)